Chapter 2
Material Properties of TiO$_2$ Nanotube Arrays: Structural, Elemental, Mechanical, Optical, and Electrical

2.1 Introduction

In this chapter, we examine the structural, elemental, crystallization, optical, electrical, and mechanical properties of the anodization-synthesized titania nanotube arrays.

2.2 Structural and Elemental Characterization

It is known that the as-fabricated nanotube arrays have an amorphous crystallographic structure. Upon annealing at elevated temperatures in an oxygen ambient, the nanotube walls transform into anatase phase, and a layer of metal underneath the nanotubes converts into rutile [1–9]; the observed crystalline phases are polycrystalline. We make note of a publication where the authors mistook the diffraction pattern of a selected small area, determined using transmission electron microscopy (TEM), as representing a single-crystal nanotube [10]. Titania properties depend on the crystallinity and isomorph type, and hence the utility of their application also varies. For example, anatase phase is preferred in charge-separating devices such as dye-sensitized solar cells (DSCs) and in photocatalysis, while rutile is used predominantly in gas sensors and as dielectric layers. Of the titania polymorphs, rutile has minimum free energy, and hence given the necessary activation energy, other polymorphs including anatase transform into rutile through a first-order phase transformation. The temperature at which metastable anatase converts to rutile depends upon several factors including the presence of impurities, feature size, texture, and strain. Hence with sintering, porosity and/or surface area reduction occur due to nucleation-growth type of phase transformations [11–13].

Glancing angle X-ray diffraction (GAXRD) patterns of a 20 V HF aqueous electrolyte sample annealed at different temperatures in dry oxygen are shown in Fig. 2.1 [1]. The anatase phase begins to appear at 280°C. As the sample annealed at

250°C was amorphous, only reflections from the titanium support can be seen, but it is clear that the sample begins to crystallize in anatase phase at a temperature between 250 and 280°C. At a temperature near 430°C, the rutile phase appears in the X-ray diffraction pattern. Beyond this temperature, the rutile (110) peak grows, whereas the anatase (101) peak from the nanotube arrays, only a few hundred nanometers long, diminishes. Complete transformation to rutile occurs in the temperature range 620–680°C. It can also be seen from Fig. 2.1 that the reflection from the titanium support is reduced at temperatures between 430 and 580°C, as the rutile barrier layer develops, fully vanishing at around 680°C.
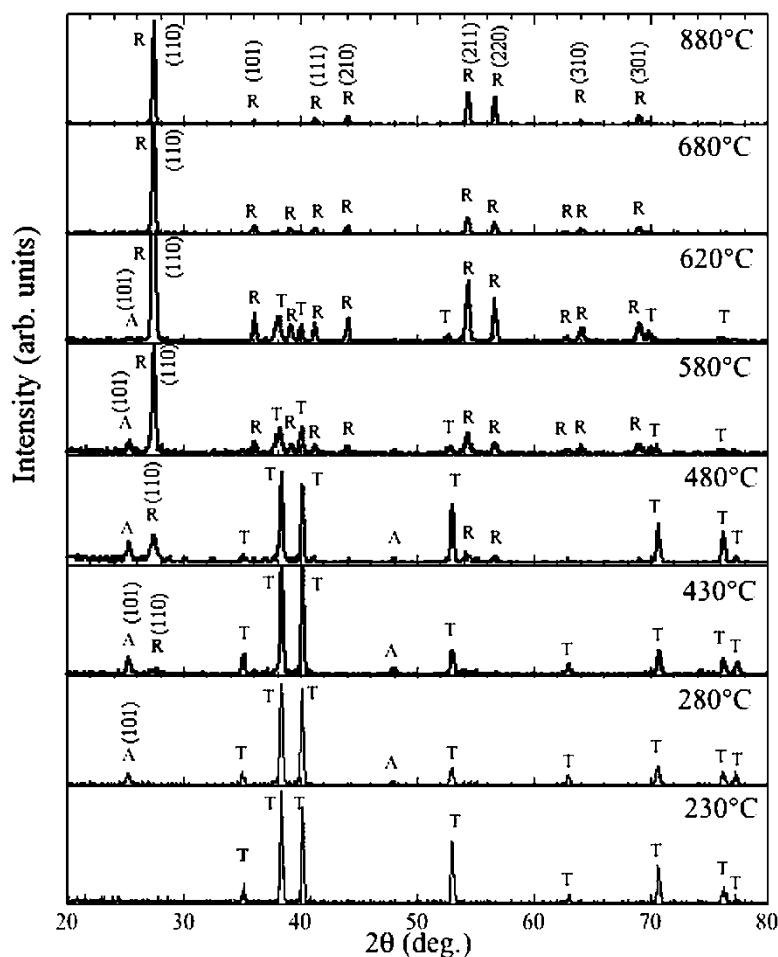

Fig. 2.1 GAXRD patterns of the nanotube samples annealed at temperatures ranging from 230 to 880°C in dry oxygen ambient for 3 h. A, R, and T represent anatase, rutile, and titanium, respectively [1]

The anatase grain size initially increases with temperature, decreasing between ~480 and 580°C, then again increasing beyond 580°C. The rutile grain size progressively increases with temperature after its nucleation. For a 3 h anneal, at 430°C a rutile fraction of 31% compared to anatase was formed, increasing to 75% at 480°C, and 92% at 580°C. For nanotube arrays atop Ti foil, 20 V HF aqueous electrolyte, the nanotube array structure was found to be stable up to around 580°C (for a slightly shorter 10-V sample, it is about 500°C). No discernible change in the pore diameter or wall thickness was observed even after annealing for 3 h at this temperature. Depending upon the sample, it was observed that at temperatures between 550 and 580°C, small protrusions, due to underlying oxide growth, come out through the porous structure. A 20-V sample was annealed in oxygen ambient to 820°C at a heating and cooling rate of 10°C/min; the tubular structure was disturbed, but porosity remained with the walls of the nanotubes coalesced to form a worm-like appearance. High-resolution TEM (HRTEM) images of the walls indicated a crystallite length of between ~35 and ~12 nm width; all wall crystallites were found to be anatase. On comparing energy dispersive X-ray spectra (EDS) of the as-synthesized nanotubes, and nanotubes fired at 580°C in an oxygen ambient, the relative intensity of oxygen peak with respect to titanium Kα peak increased on annealing in presence of oxygen, indicating improvement in the sample stoichiometry [1].

We find that thin-film samples with a continuous metal layer underneath the nanotubes behave in a way similar to that of the foil samples, with both rutile and anatase phases coexisting at 480°C. Thin-film samples with a discontinuous metal film underneath the tubes, e.g., taken out of the anodization bath at P5 of Fig. 1.33, generally show rutile but may not be as dependent upon the amount of remaining metal. These results indicate that rutile phase grows at the interface between the barrier layer and titanium metal, where the metal is thermally oxidized. The physical constraints imposed by the size of the nanotube walls make it difficult for the anatase crystals situated there to undergo phase transformation to rutile.

X-ray patterns of samples obtained in H_3BO_3–HNO_3–HF and HNO_3–HF baths, annealed at 550°C for 6 h with a heating and cooling rate of 1°C/min in oxygen ambient, are similar to the one observed for short nanotubes obtained via HF aqueous bath [14]. After annealing, the phase-structure of the architecture can be viewed as an anatase nanotube array atop a rutile barrier layer. In comparison, a TiO_2 film made by 550°C thermal annealing is primarily rutile phase with traces of anatase phase. The normalized reference intensity ratio (RIR) method was used to estimate the weight fraction of anatase, rutile, and titanium in the resulting samples [15]. The calculated RIR result of the H_3BO_3–HNO_3–HF prepared sample is anatase 33.6%, rutile 58.7%, and titanium 7.7%. The calculated RIR result of the HNO_3–HF-prepared sample is anatase 1.7%, rutile 66.5%, and titanium 31.7%. Considering a similar X-ray sampling depth for both samples, the higher weight percentage of titanium in the HNO_3–HF-anodized sample indicates a thinner barrier layer and shorter nanotube-array length.

X-ray photoelectron spectroscopy (XPS) was used to characterize the stoichiometry of as-prepared titania nanotube arrays, anodized at 20 V in an aqueous 0.5% HF electrolyte. Figure 2.2 shows the XPS spectra of Ti 2p and O 1s on the nanotube
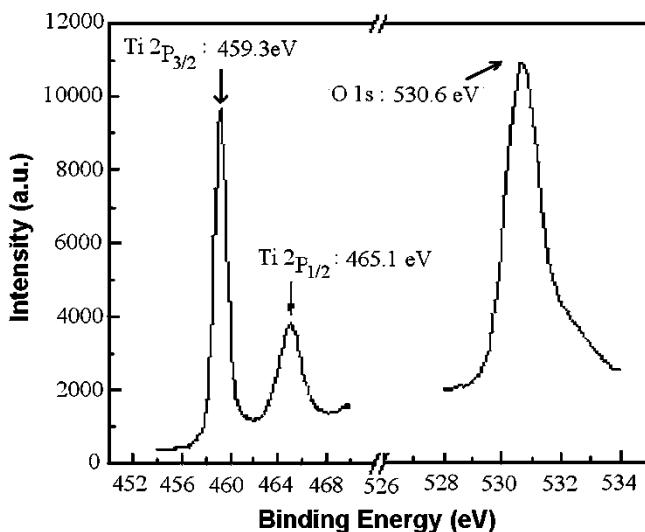
Fig. 2.2 High-resolution XPS spectra of the Ti 2p and O 1s region of as-synthesized nanotube array anodized at 20 V ([16]; Reprinted by permission of ECS –The Electrochemical Society)

array surface. Ti 2p$_{3/2}$ and 2p$_{1/2}$ peaks were observed at 459.3 and 465.1 eV, respectively [16], indicating Ti^{4+} [17]. The O 1s peak has a slightly asymmetric tail on the high-binding-energy side, which might be attributed to hydroxyl groups at the outermost surface as well as the adsorbed water resulting from moisture adsorption in air [16, 18].

A XPS scan for the HNO$_3$–HF sample, after 550°C annealing, indicated the elements Ti (23.0%), O (64.3%), N (1.0%), F (0.5%), and C (8.0%). For the H$_3$BO$_3$–HNO$_3$–HF electrolyte sample, 550°C annealed, XPS indicated Ti (27.4%), O (65.3%), N (0.3%), F (0.8%), and C (4.7%). Both carbon and some of the oxygen can be viewed as surface contaminates, while the small amounts of N and F originate from the anodization electrolytes. XPS analysis of the H$_3$BO$_3$–HNO$_3$–HF sample before annealing specifies Ti (26.9%), O (60.2%), N (1.7%), F (6.6%), and C (4.5%). Chemical state analysis indicates that the sample is comprised of Ti^{4+} bonded with oxygen (TiO$_2$), contaminated with N, F, and C compounds. The O1s spectra of the samples (in boric acid bath) showed a single peak at 530.8 eV. However, in the HNO$_3$–HF sample there is an indication of a second peak at 532 eV, revealing the presence of two forms of oxygen [14]. The Ti2p$_{3/2}$ peak has a binding energy of 459.0 eV for both samples, indicating that Ti present in the samples is in the form of TiO$_2$. For these measurements, the sampling depth of the X-rays is 8 nm, and therefore the Ti substrate cannot be detected. The position of 2p$_{3/2}$ peak is consistent with the formation of a crystalline TiO$_2$ [19, 20].

GAXRD patterns of 6-μm nanotube array samples fabricated using KF (or NaF, the two acids result in equivalent architectures) based electrolytes, with sodium hydroxide used to adjust the pH, and annealed at temperatures up to 700°C are

Fig. 2.3 Glancing angle
X-ray diffraction patterns
of a 6-µm-long nanotube
array sample as a function
of annealing temperature
(oxygen ambient) [21]
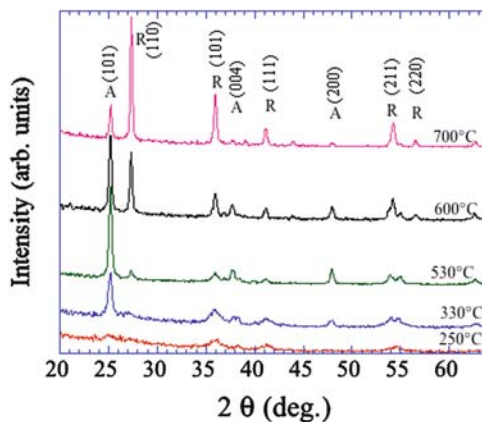
shown in Fig. 2.3 [2, 5, 21]. Crystallization occurs in the anatase phase at a temperature near 280°C, the same as for nanotube samples prepared using an HF electrolyte [1]. Electrolyte concentration and/or pH appear to have no influence on the crystallization temperature of the nanotubes. The rutile phase appears at 530°C, with the signal increasing with annealing temperature. No sign of nanotube disruption was observed in the field emission scanning electron microscopy (FESEM) images of the samples annealed at 580°C. This is in contrast with shorter nanotubes, HF grown at pH < 1, which started disintegrating at this temperature [1]. Yang and coworkers made similar observations during the crystallization of 4.2-µm-long nanotubes (pore size of 80 nm) in the temperature range 300–800°C [9], with the length and average diameter of the nanotubes showing no discernible changes after calcination up to 500°C. However, the nanotube length decreased to 3 µm after calcination at 550°C. After calcination at higher temperatures, 600 and 700°C, the length of the nanotubes decreased to 2.8 and 1.5 µm, respectively, and at the same time a thick oxide layer grew between the titanium substrate and the nanotube arrays. At 700°C, small protrusions emerged through the nanotubes, resulting in their cracking. The nanotubular structure of the samples annealed 800°C completely collapsed.

A TEM image of a single nanotube grown from a sample prepared at pH 5.0 and annealed at 600°C, see Fig. 2.4, indicates the presence of anatase, but no rutile, phase in the walls [21, 22]. The TEM data in conjunction with the GAXRD patterns confirm the crystallization model proposed in our earlier work on short nanotubes prepared using HF electrolyte [1, 3]. According to this model, anatase crystals are formed at the nanotube–Ti substrate interface as a result of elevated temperature metal oxidation. The rutile crystallites originate in the oxide layer (formed by the oxidation of titanium metal) through phase transformation of anatase crystallites existing in the region. The constraints imposed by the nanotube walls prevent anatase crystallites in the nanotube walls from transitioning to the rutile phase [2, 21, 23]. Therefore, nanotubes, annealed at temperatures between 530 and 580°C, can be considered as anatase crystallites stacked in cylindrical shape on a rutile foundation.
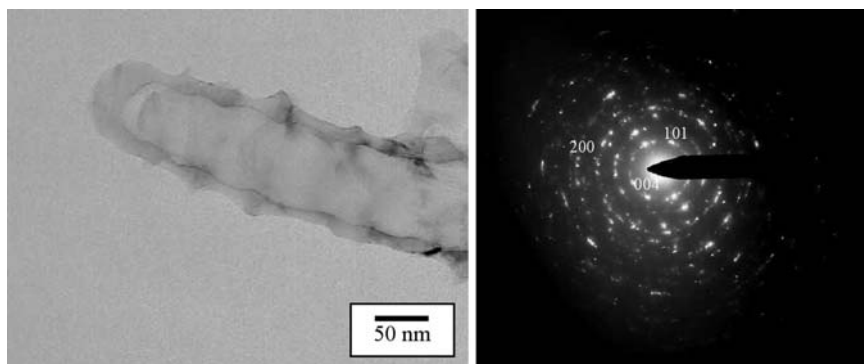
Fig. 2.4 TEM image of a single nanotube from a sample prepared at pH 5.0 and annealed at 600°C, with corresponding diffraction pattern [21]
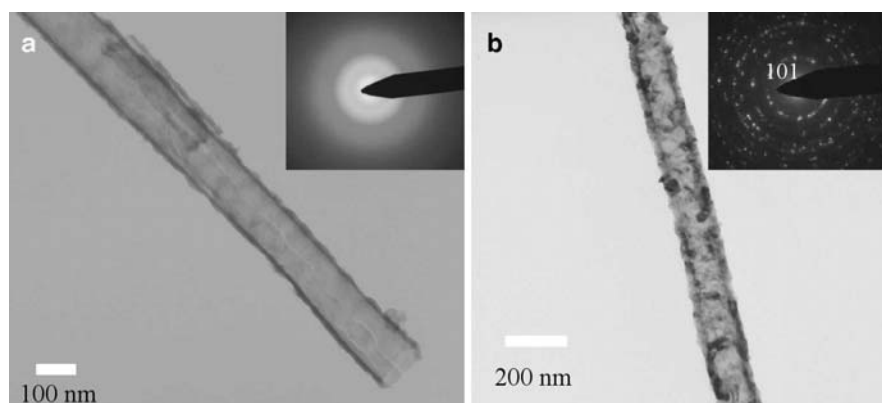
Fig. 2.5 High-resolution TEM images of DMSO 40-V nanotube sample: (**a**) as-prepared, and (**b**) after 550°C anneal in oxygen for 6 h. The corresponding selected area diffraction patterns are given in the *insets* [24]

Figure 2.5 shows HRTEM images of a portion of a nanotube~45 µm long grown at 40 V in DMSO containing 2% HF [24]. Figure 2.5a is an image of an as-prepared nanotube, and Fig. 2.5b that of a nanotube annealed at 550°C in oxygen. The corresponding diffraction patterns from the nanotubes are given in the inset. Clearly, the as-prepared nanotubes are amorphous. Consistent with the earlier studies regarding the nanotube array crystallization [1], the sample annealed at 550°C shows only the anatase phase in the nanotube's walls. GAXRD analysis confirms the TEM studies that the as-anodized samples are amorphous. Figure 2.6 is GAXRD of a 40-V ethylene glycol, 14-µm-long 4-h 580°C annealed nanotube array sample exhibiting anatase peaks [24, 25]. While the barrier layer underlying the nanotube array remains rutile [1], no rutile can be seen in the spectra since the tubes are of such great length. Identical GAXRD spectra are obtained for any of the nanotube array samples fabricated using the polar organic electrolytes described in Chap. 1.
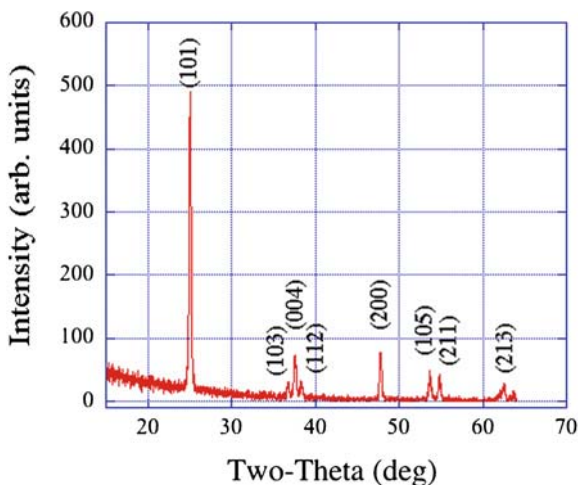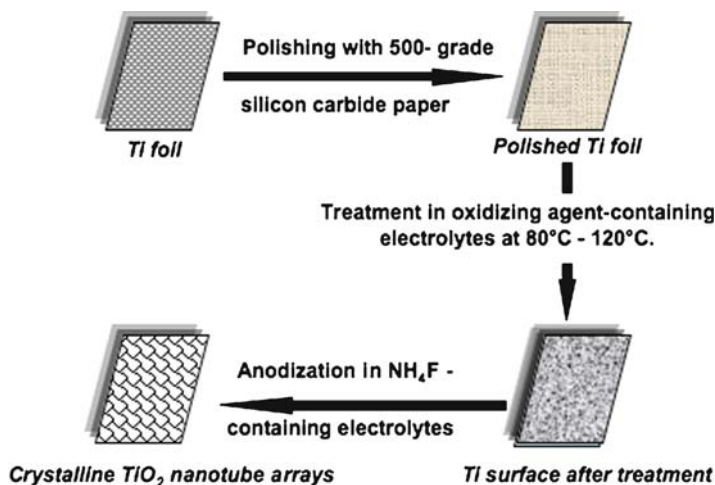
Fig. 2.6 GAXRD pattern of a nanotube array sample anodized at 40 V in an ethylene glycol electrolyte containing 0.25% wt NH$_4$F, annealed in oxygen at 580°C for 4 h [24]

## 2.2.1   *Anodic Formation of Crystalline Metal Oxide Nanotubes*

Highly crystalline structures offer unique advantages over amorphous architectures by providing a direct and rapid pathway for charge transport, thus decreasing the carrier path length, which in turn reduces recombination losses [27, 28]. The need for high-temperature crystallization limits the use of nanotube arrays with temperature-sensitive materials, such as polymers. One approach to achieving crystalline nanotube arrays is to start with a crystalline layer, and then anodize the film to achieve crystalline nanotubes [26]. Titanium foil samples were first treated with an oxidizing agent-containing electrolyte, e.g., H$_2$O$_2$ at 80°C or (NH$_4$)$_2$S$_2$O$_8$ at 120°C, then anodized at constant voltage in a fluoride-containing electrolyte [26]. A schematic of this two-step process is shown in Fig. 2.7. The two steps are not symmetrical; treating as-synthesized amorphous TiO$_2$ nanotube arrays with the oxidizing agent-containing electrolyte destroys the nanotubes.

   After the initial treatment of the Ti foil sample in a peroxide electrolyte at 80°C, the resulting films were then anodized in aqueous solutions containing NH$_4$F [26]. Figure 2.8 shows the GAXRD results for an as-anodized sample. The inset of Fig. 2.8 shows an FESEM top-view image of the nanotube array architecture. Figure 2.9a shows a TEM micrograph for a similarly fabricated nanotube array sample, and Fig. 2.9b the corresponding diffraction pattern which indicates a best fit to anatase. Figure 2.9c gives the intensity from a rotationally averaged pattern with expected Bragg lines from anatase [26].

   The 80°C peroxide pretreatment of the Ti foil produces a crystalline oxide layer~1.2 μm thick. Subsequent anodization in a fluoride-containing electrolyte

Fig. 2.7 Schematic presentation of the two-step fabrication process used to directly synthesize crystalline TiO$_2$ nanotube arrays [26]
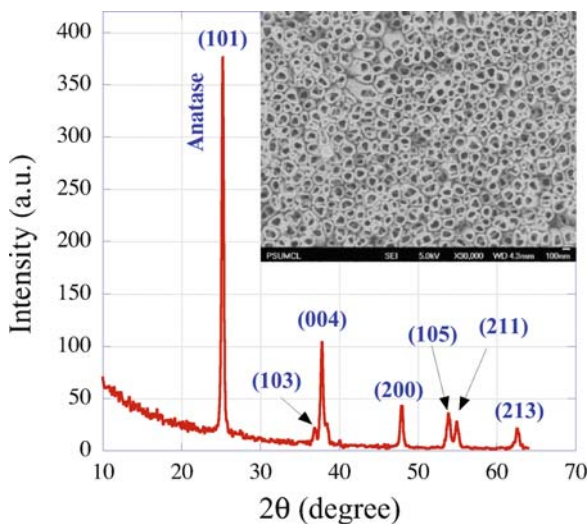
Fig. 2.8 GAXRD pattern of well-developed nanotube arrays formed by anodizing a peroxide-treated Ti foil sample in an aqueous electrolyte containing 0.25 M NH$_4$F+0.1 M H$_3$PO$_3$+0.05 M H$_2$O$_2$;the *inset* shows a FESEM top-view image of this same sample [26]

initially produces a crystalline nanotube array structure by structuring of the crystalline oxide layer. As the anodization continues with time, due to field-assisted oxidation and dissolution, as well as chemical dissolution, the Ti–oxide interface gradually moves deeper into the Ti metal and the outer surface dissolves. Therefore, with increasing anodization duration (longer than 3 h) the nanotube growth
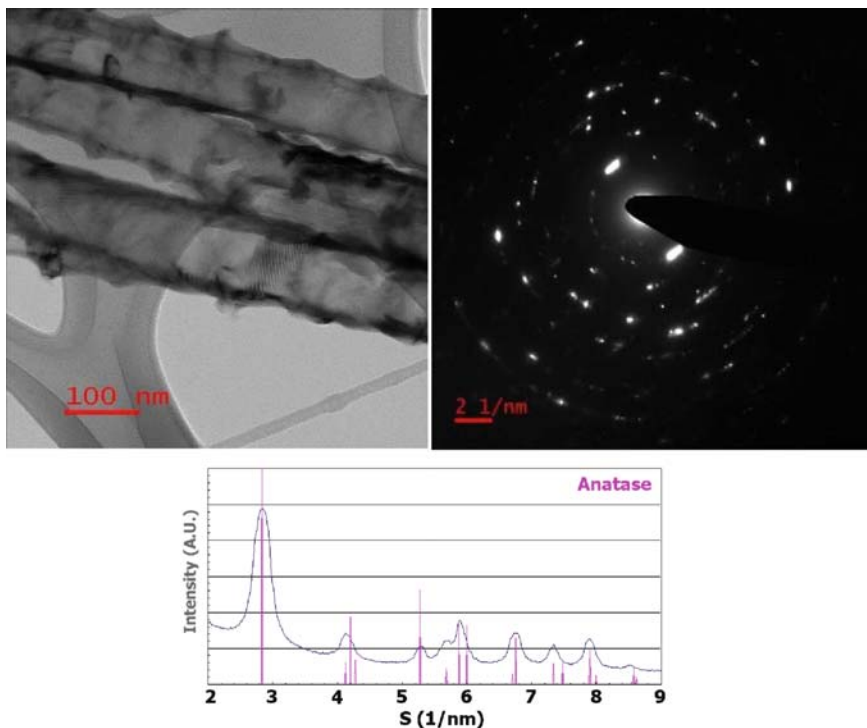
Fig. 2.9 (**a**) TEM image of nanotubes formed by described technique; (**b**) corresponding selected area diffraction pattern; and (**c**) intensity from rotationally averaged pattern compared with expected Bragg lines for anatase [26]

proceeds through the crystalline oxide layer initially present, and is then replaced with an amorphous nanotube array structure; hence the GAXRD-observed crystallinity of the nanotube arrays decreases for extended anodization durations. This anodization time restriction limits the crystalline tube length to about 800 nm. Strategies to overcome this limitation include the use of stronger oxidizing agents to produce a thicker crystalline oxide layer, which is then converted into nanotubular architecture by subsequent anodization. To this end, we immersed Ti foil samples in ammonium persulfate, $(NH_4)_2S_2O_8$, which is a stronger oxidizing agent, at 120°C for 3 h. The 120°C ammonium persulfate pretreatment of the Ti foil produces a crystalline oxide layer approximately 1.6 μm thick; temperatures lower than 120°C resulted in thinner films, and higher temperatures resulted in an insulator-like film which we were unable to anodize. Subsequent anodization of the resulting samples in aqueous solutions containing NH_4F enables fabrication of nanotube arrays 1.4 μm in length. Figure 2.10 shows the GAXRD results for an as-anodized persulfate sample, indicating that the nanotube arrays are largely anatase, and the inset of Fig. 2.10 shows an FESEM top-view image of the nanotube array architecture achieved with the persulfate sample [26].
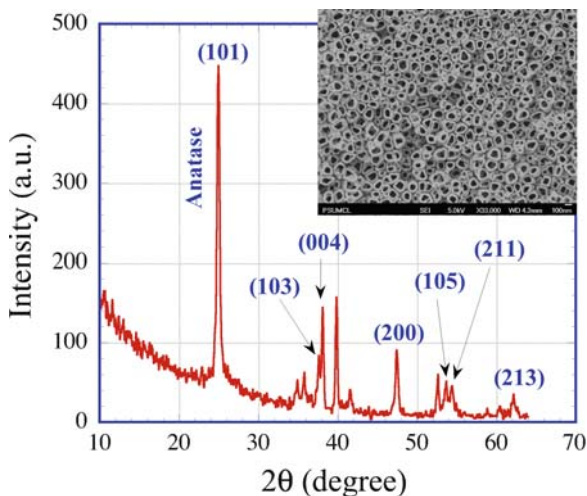
Fig. 2.10 GAXRD pattern of well-developed nanotube array sample formed by anodizing a persulfate-treated Ti foil sample in an aqueous electrolyte containing 0.25 M NH$_4$F+0.1 M H$_3$PO$_3$+0.05 M H$_2$O$_2$; *inset* shows FESEM top-view image of similar sample [26]

## 2.2.2   Improved Crystallization via Solvothermal Treatment

Thin-wall nanotube array architectures offer high surface area, facile diffusion of the photogenerated holes to the electrolyte, and directed charge transfer of the photo-generated electrons to the back contact for hydrogen evolution [29]. A high degree of crystallization appears a prerequisite for useful photocatalytic materials, with crystallinity playing a key role in charge separation and transport [30, 31]. In general, higher crystallinity implies fewer amorphous regions and grain boundaries, and hence a lower density of trap states. The anodically grown titania nanotube arrays are amorphous and hence exhibit negligible photocatalytic activity. High-temperature crystallization anneals, in an oxygen ambient to maintain stoichiometry, result in the growth of a dense rutile layer from the metal film underlying the nanotube arrays, introducing a significant series resistance that hinders transport of the photogenerated electrons to the back contact [4]. Solvothermal methods are well known for crystal size enhancement [32, 33]. Reactions take place in a closed system under autogeneous pressure, which can be varied by choice of solvent, reaction temperature, and volume filling of the reaction vessel [34, 35]. When solvothermal treatments were performed on water-immersed titania nanotube array samples, we observed disorientation of the vertically aligned nanotubes and detachment of the tubes from the underlying substrate. These problems were eliminated when ethanol [36, 37]was used instead of water, with the samples exposed to the resulting ethanol vapor rather than keeping them in physical contact with the liquid medium.

The ethanol vapor treatment was carried out in a 23-ml Teflon-lined stainless steel chamber. Optimal enhanced crystallization conditions were found with a

Fig. 2.11 GAXRD of (**a**) ethanol vapor-treated titania nanotube array sample; (**b**) as-anodized amorphous titania nanotube array sample
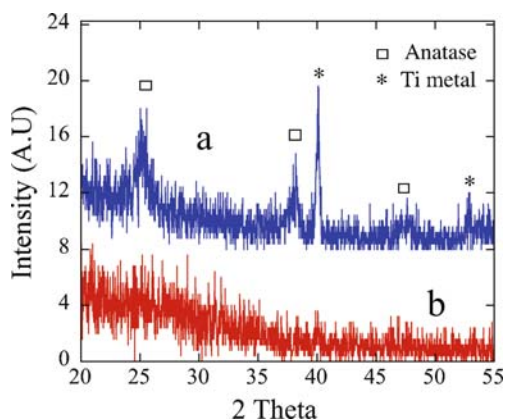
Fig. 2.12 GAXRD patterns of (**a**) 580°C annealed titania nanotube array sample without solvothermal treatment; (**b**) sample thermally annealed and then subjected to ethanol vapor treatment
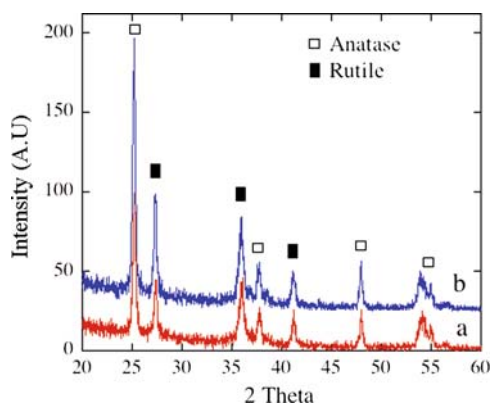

reaction temperature of 140°C and 25% filling volume, corresponding to a reaction chamber pressure of approximately 50 psi. Hence for the treatment of all samples, 6 ml of ethanol was placed within the Teflon beaker, with the nanotube array sample mounted on the top of a grooved Teflon stub to avoid direct contact with the liquid medium. The sealed chamber was then kept at 140°C for 18 h.

Figure 2.11 shows the GAXRD patterns of an as-anodized titania nanotube array sample and a similar sample after being subjected to the ethanol vapor treatment. It is evident that the 140°C vapor treatment results in some minimal degree of crystallization. Figure 2.12 shows the GAXRD patterns of a thermally annealed sample and a vapor-treated, thermally annealed sample (samples of the same dimensions and identical instrument conditions were used for recording the spectra). The patterns from both samples show identical peak positions and the presence of both anatase and rutile phases. All major reflections from the vapor-treated, thermally annealed sample are stronger than those of the untreated sample, indicating a significant increase in the degree of crystallization with the ethanol vapor treatment.

2.2.3   Partially Crystalline Anatase Phase Nanotubes by Anodization

As-synthesized nanotube arrays are commonly amorphous. Hence Fig. 2.13, which is the GAXRD pattern of an as-anodized sample prepared from DEG+0.5 wt% NH$_4$F+2% H$_2$O electrolyte anodized at 80 V for 48 h at room temperature, is of considerable interest since the anatase (101) peak indicates partial crystallization of the tubes [38]. The anatase (101) intensity significantly increases with an increase of NH$_4$F concentration to 0.9 wt%, with a distinct anatase (004) peak, see Fig. 2.14. However, at this higher NH$_4$F concentration, the electrolyte is not able to maintain the nanotube structure, and only flakes are obtained.

To achieve the nanotube structure in crystalline form, optimization of a combination of anodization parameters is required. Crystallization is strictly determined by migration of Ti^{4+} outward from the substrate and O^{2-}/OH$^-$ inward to form crystalline oxide in a ratio that favors crystal growth [39]. Additionally, because crystallization of anodic titania can be correlated with ionic transport during the film growth [40, 41], it appears that the chemical properties of the solvent
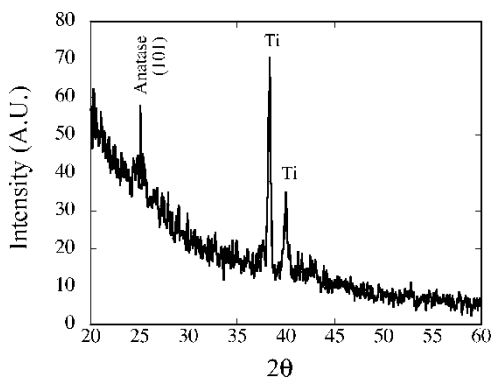
Fig. 2.13 GAXRD pattern of an as-anodized sample obtained from DEG –0.5 wt% NH$_4$F–2%H$_2$O electrolyte at room temperature [38]
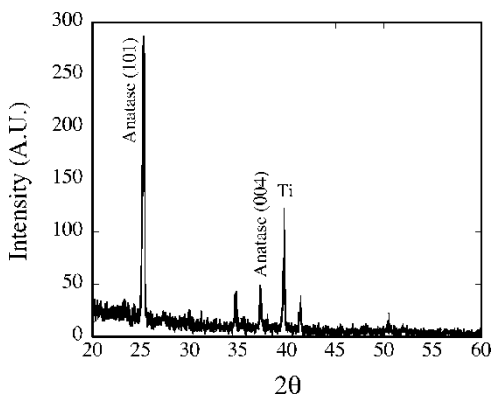
Fig. 2.14 GAXRD pattern of an as-anodized sample obtained from DEG –0.9 wt% NH$_4$F–2%H$_2$O electrolyte at room temperature [38]

diethylene glycol, such as inter- and intra-molecular hydrogen bonding [42, 43], and its physical properties, such as viscosity, play an as yet undetermined role.

2.3 Characterization of Doped Titania Nanotubes

Titania nanotube arrays appear a useful catalyst, under bandgap illumination, for water photoelectrolysis [44–48]. Semiconducting TiO_2 (3.2 eV bandgap) absorbs UV light, which comprises only~4% of the solar energy spectrum. Means to shift the absorption properties of TiO_2 have historically focused on sensitization of the TiO_2 with low bandgap semiconductors having suitable energy level positions with respect to that of TiO_2, or by doping with foreign elements such as C, N, F, B, P, and S [49–53].

2.3.1 Carbon Incorporation Within the Nanotubes

Park et al. prepared carbon-doped titania ($TiO_{2−x}C_x$) nanotubular arrays by reduction of carbon monoxide [45]. Raja et al. reported $TiO_{2−x}C_x$ nanotubular arrays prepared by acetylene reduction [46]. Hahn et al. treated the nanotubes at 500°C under a mixed flux of N_2 and acetylene to incorporate carbon [49]. Mohapatra and coworkers reported carbon-doped titania nanotube arrays prepared by the sonoelectrochemical anodization method using an ethylene glycol–ammonium fluoride solution and annealing the as-anodized sample under reducing atmosphere (H_2), which converts the amorphous nanotube arrays to photoactive anatase phase as well as helps in doping of the carbon (from the reduction of ethylene glycol) to give the $TiO_{2−x}C_x$-type photoanode [50, 54]. Shankar and coworkers subjected nanotube arrays to a flame annealing process [55]; an XPS scan of these samples revealed the presence of carbon in all samples; a summary of the carbon content and carbon state information is provided in Table 2.1 [55]. Fluorine was present in all samples, at

Table 2.1 Carbon content and chemical state information (from XPS) of flame annealed TiO_2 nanotube arrays [56]

Sample	Depth (nm)	Total C (atom%)	C–C	C–O	COO
Short NT	0	0.7	–	–	–
	100	0.3	–	–	–
Flame-annealed short NT	0	3.3	2.5	0.4	0.5
	100	2.8	1.9	0.6	0.3
Flame-annealed long NT	0	5.6	3.9	0.8	0.9
	100	5.2	3.8	0.9	0.6
Long NT	0	3.5	2.3	0.5	0.7
	100	3.0	1.9	0.6	0.5
Flame-annealed Ti foil	0	4.0	2.7	0.6	0.7
	100	3.8	2.5	0.7	0.5

a surface concentration of nearly 2 atomic%, decreasing to about 0.2 atom% in the interior [56]. Based on the analysis of the C1s peak, incorporated carbon was present in C–C (285.3 eV), CO (286.5 eV), COO (289.0 eV), and C–N bonds. The Ti–C signal at 281.9 eV was not observed. The carbon content of the short nanotubes, which is initially quite small, becomes appreciable upon flame annealing [55]. A significant amount of carbon (~3%) is present in the long nanotube sample even prior to flame annealing, which is attributed to the presence of a large number of organic ions such as citrate and tetrabutylammonium in the anodizing bath. In long nanotubes, flame annealing introduces additional carbon into a structure where carbon pre-exists in appreciable quantities. Hence, flame-annealed long nanotubes have the highest carbon content (>5%) of the samples studied. While these various routes, and those mentioned below, are able to dope the titania nanotube arrays, the resulting photocurrents offer no significant improvement beyond TiO₂.

2.3.2   Nitrogen Incorporation Within the Nanotubes

Substitutional N-doping has been suggested as a route for lowering the bandgap of titania [56–59]. Nitrogen ions substitute oxygen atoms in the TiO₂ lattice and thus the corresponding N(2p) states are located above the valence band edge. Mixing of N(2p) states with O(2p) states results in a reduction of the bandgap of the N-doped TiO₂. Common approaches to achieving N-doped TiO₂ nanotubes are N₂/H₂ gas plasma treatment, annealing in ammonia gas, N-ion bombardment, N-ion doping during the fabrication of nanotubes via anodization, etc. [52, 60–63].

Efforts have been made to nitrogen dope nanotube arrays in situ during the growth and fabrication of nanotubes [63]. Titanium foils were potentiostatically anodized at 25 V in an electrolyte of pH 3.5 containing 0.4M ammonium nitrate NH₄NO₃ and 0.07M HF acid; with reference to Fig. 2.15, Sample A was removed after 17 s of anodization, while Sample B was anodized for 240 s. Sample C was
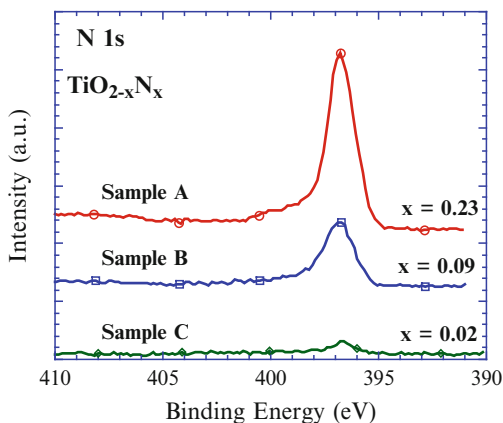
Fig. 2.15 N 1s XPS spectra for samples A–C with respective nitrogen doping levels [63]

anodized for 6 h at 20 V in an electrolyte of pH 3.5 containing 2.5M NH_4NO_3 and 0.07M HF. Such anodization chemistry restricts the electrolytic ions to nitrogen and fluorine bearing species, allowing control of the possible elements that can be incorporated into the anodic titania films. The potential and pH regimes chosen were such as to facilitate nanotube array formation. The maximum current at the onset of the anodization was limited by the compliance of the power supply used to perform the anodization. In the first 25 s after application of the voltage, the measured current density reduced from 4,120 mA/cm^2 to a local minimum between 15 and 25 mA/cm^2, with the field-assisted oxidation of the Ti metal surface reducing the current. In the potential range under consideration, this behavior is typical for the anodization of Ti in fluoride ion-containing acidic electrolytes; however, the magnitude of the anodization currents is much greater. The larger anodization currents are attributed to the stronger oxidizing and etching action of the nitrate ion-containing electrolyte. High-resolution N 1s XPS spectra of Samples A ($x=0.23$), B ($x=0.09$), and C ($x=0.02$) (see [63])are shown in Fig. 2.15. XPS data confirm that all the incorporated nitrogen is substitutional on the oxygen site. The nitrogen peak at 396.8 eV was observed and assigned to atomic β–N, indicating a chemically bound N^- state [64, 65]. Fluorine was present in the amorphous as-anodized samples, with the final concentration of incorporated F^- sensitive to the annealing conditions. Annealing processes (in air) lasting longer than 6 h at temperatures above 600°C resulted in fluorine atoms being completely resubstituted by oxygen. The depth profile of a 250-nm-thick film with a surface nitrogen concentration $x=0.05$ (the sample was anodized at 20 V for 120 s in a pH 4.5 electrolyte containing 0.4 M ammonium nitrate and 0.07 M hydrofluoric acid then annealed per the other samples) indicated that the nitrogen doping is inhomogeneous with the maximum nitrogen being incorporated close to the surface, and then linearly decreasing with increasing depth inside the film. The precise reactions involving the decomposition of ammonium ions and nitrate ions at the anodic surface to form N-doped titania are unclear. However, the anodization of aluminum in nitric acid has been studied previously and is known to be relatively complex [66]. A study of the interaction of aluminum with nitrate ions in thin oxide films formed in nitrate ion-containing electrolytes indicated that the adsorption of nitrate ions on the oxidized surface of aluminum was followed by their reduction inside the oxide film [67]. Parhutik and coworkers [68] reported the incorporation of electrolyte anions in the anodic film formed by anodization of Al in HNO_3 solution. Furthermore, it was reported that the anion concentration in the growing oxide reaches a maximum value at the moment when intensive pore growth starts and the oxide is thin, i.e., when the anodizing time is very brief [66, 68]. Similar behavior was observed for Ti anodization, with maximum nitrogen incorporation occurring in a film anodized for a mere 17 s (Sample A). Thus, a trade-off exists between the morphology and the level of nitrogen doping. Shorter anodization periods result in higher concentrations of incorporated nitrogen, whereas longer anodization periods are required for evolution of the nanotube-array architecture.

Nitrogen doping by ion implantation of self-organized anodic titania nanotubes combined with a subsequent anneal to remove induced defects has been

investigated [61, 62, 69]. Ochsner et al. [69] formed nanotube array films in a H_2SO_4/HF electrolyte, which were then annealed to an anatase structure, implanted with nitrogen using ion bombardment at 60 keV and a nominal dose of 1×10^{16} ions/cm^2, and then finally re-annealed to anatase. Images do not show any detectable morphological difference with the different steps. XRD results presented for the films before doping, after nitrogen implantation, and after re-annealing showed that ion implantation leads to amorphization of the structure and that re-annealing at 450°C for 3 h recovers the structure to anatase [61]. XPS spectra of the implanted TiO₂ tubes exhibited N 1s peaks in the implanted and annealed nanotube layer (annealed at 450°C for 3 h) after 20 nm by Ar$^+$ sputtering [61]. Two peaks were distinguished: one at 400 ± 0.2 eV and another one at 396 ± 0.2 eV. The peak detected at 400 eV is assigned to a well-screened γ–N state (essentially adsorbed N), and the one detected at 396 eV is assigned to an atomic β–N state such as TiN [70].Therefore, one can deduce from XPS results that nitrogen is successfully implanted in the structure in a chemically bonded state.

2.3.3 Boron-Doped Nanotubes

Boron doping was reported by use of electrodeposition, where the anodized nanotube sample was subjected to a current density of 10 μA/cm^2 for 27 min in a 0.1 M H_3BO_3 electrolyte [53, 71]. XPS spectrum showed B 1s peak at 191.4 eV for the boron-doped sample. According to the standard B 1s binding energies in TiB₂ (187.5 eV, Ti–B) and B_2O_3 (193.0 eV, B–O) [72], the B 1s binding energy of 191.4 eV might be assigned to the mixed state Ti–O–B of TiB₂ and B_2O_3, which is consistent with the published value of the B 1s signal for boron-doped TiO₂ in XPS analysis [71–73].

2.3.4 Organic Bath

XPS was used to determine the elemental composition of the nanotube array samples fabricated in an organic anodization bath, and results are summarized in Table 2.2 [74]. The nanotube array samples are predominately titanium and oxygen, with traces of fluorine and sulfur due to solvent incorporation in the anodic films. It was

Table 2.2 XPS results of titanium etched in fluorinated 1:1 DSMO and ethanol at 20 V for 48 h, one of the samples annealed at 550°C for 6 h [74]

Atomic con. (%)	Ti	O	F	N	C	S
Nanotubes	23.9	53.4	13.7	0.9	6.8	1.1
Annealed nanotubes	26.6	64.3	1.6	0.5	5.8	1.2

believed that surface contamination is the likely source for the nitrogen and carbon found in the samples. Chemical state analysis for titanium indicates that the sample is Ti^{4+} bonded with oxygen (TiO_2). Compared with samples fabricated in aqueous electrolytes, the atomic concentration of fluorine (13%) is considerably increased using the organic electrolyte [74]. However, the fluorine concentration is dramatically reduced in the annealed samples, falling to 1.6%; GAXRD gives no indication of TiO_xF_y or TiO_xS_y in the samples. Hence, while the results of XPS and XRD indicate a considerable amount of solvent is trapped in the amorphous anodic films, the trapped elements such as F, C, and S do not enter the rutile or anatase lattice.

2.3.5   *CdS-Coated Nanotubes*

In the GAXRD pattern of CdS-coated TiO_2 nanotube array films (HF fabricated, a few hundred nanometers in length) annealed at 350°C for 1 h, Chen and coworkers [75] observed a prominent TiO_2 Bragg peak along with weak Bragg reflections at 2θ values of 26.55, 30.75, 44.04, 52.16, and 54.67°, corresponding to the (111), (200), (220), (311), and (222) Bragg reflections of cubic CdS, respectively. The general scan spectrum of XPS of CdS–TiO_2 electrodes showed sharp peaks for Ti, O, Cd, S, and also C. The Cd 3d core level XPS spectrum has two peaks at 405.3 eV ($3 d_{5/2}$) and 411.9 eV ($3 d_{3/2}$), which are in good agreement with published values [76]. The S 2p core level spectrum indicated that there are two chemically distinct species in the spectrum. The peak at 161.9 eV is for sulfide, the structure occurs because of a split between $2p_{3/2}$ and $2p_{1/2}$; the split is near 1.18 eV and the area ratio is 2:1, in excellent agreement with published values of the S 2p signal for CdS [14]. Measured atomic concentrations of the as-prepared samples suggest that when the sulfate/O ratio is 1, the sulfide/Cd ratio is 0.86; this means that the CdS nanoparticles obtained are slightly Cd rich, which is expected for CdS under normal synthesis conditions [77].

2.4   **Optical Properties of Titania Nanotubes Arrays**

2.4.1   *Finite Difference Time Domain Simulation of Light Propagation in Nanotube Arrays*

Titania nanotube arrays can be grown over a wide range of pore diameters, wall thicknesses, and lengths, and with each topology showing different light absorption and photocatalytic properties leading to different values of photoconversion efficiency [78, 79]. Knowledge of the light absorption properties of the various nanotube-array geometries prior to sample fabrication would be desirable. Therefore, the electromagnetic computational technique known as *finite difference time*
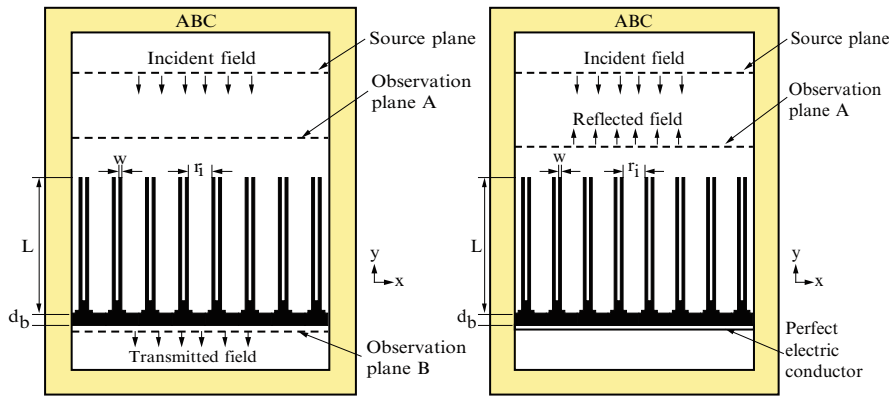
Fig. 2.16 Geometry of two-dimensional FDTD models used for determining the propagation of a transverse electromagnetic (TEM) wave through: (**a**)aself-standing titania nanotube array film (Type-I), and (**b**) titania nanotube array film on titanium substrates (Type-II) [81]

domain (FDTD) was used to simulate the light-absorbing properties of the nanotube arrays as a function of feature size and wavelength [80, 81]. The simulations were performed for titania nanotube array films with no metal layer underneath the nanotubes (transparent, Type-I) and also for the nanotubes grown on titanium foil (opaque, Type-II). Note that in the former case, Type-I, the glass substrates were not included in the simulations and hence the nanotube film can be considered self-standing. Figure 2.16 shows, respectively, the two models used to represent self-standing titania nanotube array films (transparent, Type-I) and nanotube array films on titanium foil (opaque, Type-II). The distance between two adjacent tubes was taken as 10 nm. The FDTD space was terminated with an absorbing boundary condition (ABC) made of a uniaxial perfect matching layer [82] to eliminate the reflection of any fields from these boundaries. The Type-II (Fig. 2.16b) model contains a perfect electrical conducting layer at the bottom of the nanotube array to represent the titanium layer. Therefore, in the case of Type-I, transmittance and in the case of Type-II, reflectance are used to determine the absorbance of light by the nanotube array. In all simulations reported to date, the distance between two adjacent tubes was taken as 10 nm. The validity of the FDTD simulations were established by comparison of the calculated and experimentally measured transmittance of a Type-I film of different porosities, see Fig. 2.17.

The measured absorbance spectrum of a titania nanotube array (200 nm length, 22 nm pore, 13 nm wall thickness, and 100 nm barrier layer thickness) was compared with the simulated results [83]. Both curves were found similar, except that the absorption edge of measured spectra is shifted slightly to the higher wavelength region compared to the simulated spectra. This is due to the fact that the barrier layer has rutile crystallites and the nanotube walls consist of anatase crystallites. The bandgap of the rutile is lower (3.0 eV) compared to the anatase (3.2 eV). The rutile phase at the barrier layer leads to the shifting of the absorption edge to higher wavelength, a property not taken into account by the FDTD simulations.
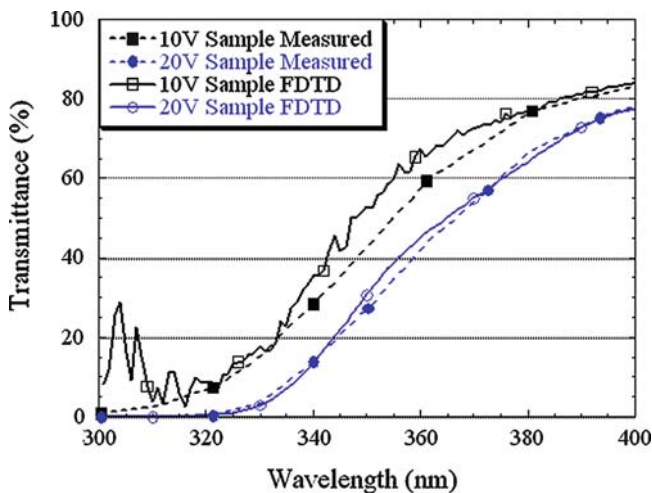
Fig. 2.17 Measured and FDTD calculated transmittance of a Type-I film made using different anodization voltages. The 10-V sample is 200 nm long, and the 20-V sample is 360 nm long [81]

As an informative demonstration, Fig. 2.18 shows the propagation of a transverse electromagnetic (TEM) wave through a titania nanotube array on Ti foil (Type-II). A derivative Gaussian wave (center frequency $= 8 \times 10^{14}$ Hz, bandwidth $= 2 \times 10^{14}$ Hz) is used as the excitation source. The tube length, pore diameter, wall thickness, and barrier layer thickness are, respectively, 1,000, 100, 20, and 100 nm. Figure 2.18a shows the wave originating from the source and moving towards the nanotubes. When the wavefront hits the top surface of the nanotube array, Fig. 2.18b, most of the incident energy is transmitted into the nanotubes, with a negligible portion reflecting back. The reflected wave can be seen in Fig. 2.18b, c as a faint horizontal line on the top of the nanotubes. The wave dissipates as it travels through the nanotube array to reach the barrier layer, Fig. 2.18c. Figure 2.18d–f shows the wave reflecting back from the conducting Ti layer at the bottom of the nanotube array. Note that the reflected wave contains multiple wavefronts, as the derivative Gaussian pulse contains radiation over a wide frequency range; the individual frequencies travel at different velocities through the barrier layer and nanotube array due to the frequency-dependent variation in the titania permittivity.

With respect to the applied properties of Type-II samples, it should be noted that to induce crystallinity the nanotube array samples are annealed at elevated temperatures in an oxygen environment. The diffusion of oxygen into Ti foil is consistent with the Fick's second law, and hence a gradient in the oxide composition exists from the top of the barrier layer to the Ti metal [83]. Consequently, there is a gradient in the complex permittivity spectrum of the oxide layer underneath the nanotubes and hence light is bent before it is reflected back from the metal. This gradient was considered during the simulation process by linearly increasing the permittivity values of the barrier layer; so the permittivity at the bottom of barrier layer is 10 times larger than at the top. Hence when light is reflected back from the
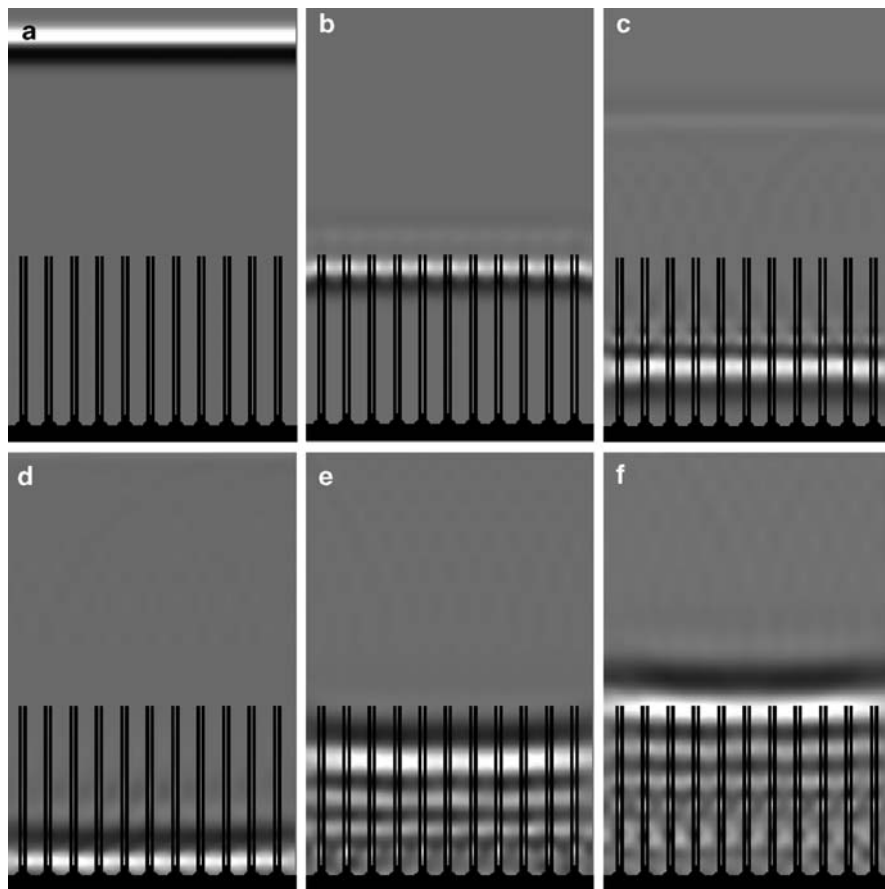
Fig. 2.18 Propagation of light through Ti-foil backed titania nanotube array at (**a**) 4.67, (**b**) 9.34, (**c**) 11.68, (**d**) 14.01, (**e**) 16.35, and (**f**) 17.51 fs (femtoseconds). The variation in field strength is represented by the different shades of gray [81]

metal, it is more readily absorbed, and therefore the intensity of the rejected light is very low, on a unit length basis, compared to that of the transmitted wave in Type-I samples. As a result, a clear difference in the absorbance can be seen between the Type-II samples (Fig. 2.19) and the Type-I samples (Fig. 2.20) [81]. The increased light absorption in Type-II samples makes them more suitable for water photolysis experiments, while the Type-I samples are better suited for application in solar cells.

The transmittance of light through self-standing TiO_2 nanotube array films (Type-I) is calculated as a function of tube length while keeping wall thickness, pore diameter, and barrier layer thickness constant. Figure 2.21 plots the transmittance of the film as a function of excitation wavelength and tube length for nanotubes of length 200 nm, pore size 22 nm, and barrier layer thickness 100 nm. The transmittance reaches a value over 95% at wavelengths greater than 380 nm.

Fig. 2.19 Absorbance of titania nanotube films as a function of tube length for arrays grown on Ti foil (Type-II); the inner diameter of the tube is 20 nm, wall thickness 10 nm, and barrier layer thickness 100 nm
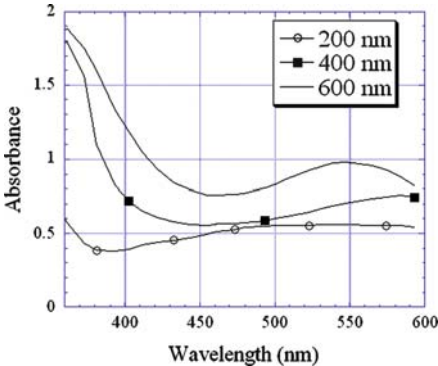
Fig. 2.20 Absorbance of titania nanotube films as a function of tube length for arrays grown on Ti foil (Type-I); the inner diameter of the tube is 20 nm, wall thickness 10 nm, and barrier thickness 100 nm [81]
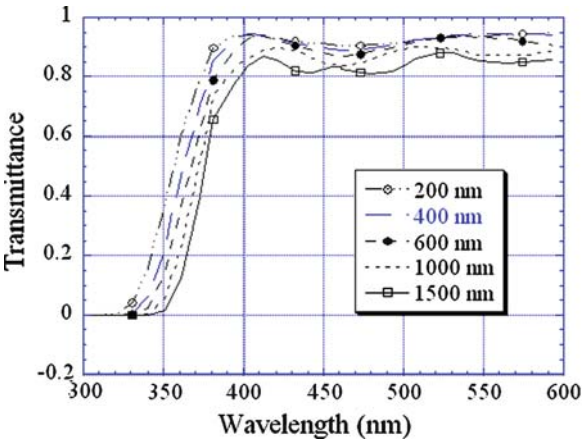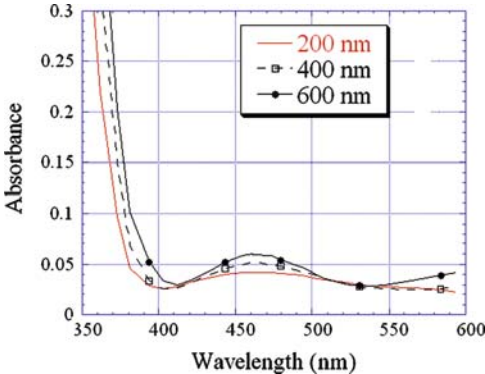
Fig. 2.21 Transmittance of TiO_2 nanotube array films as a function of tube length (Type-I; tube's inner diameter is 20 nm, wall thickness 10 nm, and barrier thickness 100 nm) [81]

The spacing between the interference patterns, created by the interaction of the transmitted wave and the wave reflected back from the top of the nanotubes, reduces with increasing nanotube length [84–86]. In the region below about 330 nm, the absorption is so high that the nanotube length has little influence. Here the light is completely absorbed by the nanotubes within a path length of a few tens of nanometers. Above this wavelength region, the transmitted fields depend on the nanotube length. It was found that for a given nanotube length, wall thickness, and barrier layer thickness, the transmittance increases slightly with increasing pore size. With the increase in porosity, the air column volume increases and the solid material volume decreases, yielding reduced effective refractive indices.

2.4.2 Measured Optical Properties

Figure 2.22 shows the transmittance spectrum of a transparent titania nanotube array film on a glass substrate [3]. The optical behavior of the TiO$_2$ nanotube arrays are quite similar to those reported for mesostructured titanium dioxide [87–89]. The difference in the envelope magnitude encompassing the interference fringe maxima and minima is relatively small compared to that observed in titania films deposited by rf sputtering, e-beam, and sol-gel methods [90–92].

The absorbance (or optical density) of the films were estimated from the transmittance T using the relation: $A = -\log(T)$. Here, we assumed that all the incident light is either transmitted or absorbed, with reflection or scattering being negligible. The Napierian absorption coefficient of the sample was calculated using
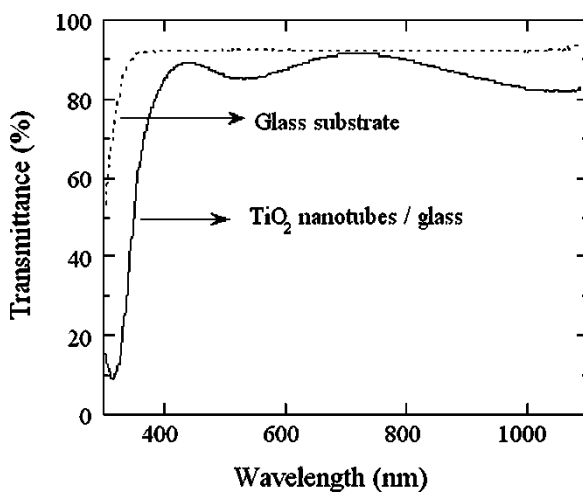
Fig. 2.22 Transmittance spectra of glass (Corning 2947) substrate, and 450°C annealed nanotubular titania film atop the same glass (Corning 2947) substrate [3]

Lamberts law, where d is the thickness of film, which can be determined using the relation

$$d = \frac{\lambda_1 \lambda_2}{2[\lambda_2 n(\lambda_1) - \lambda_1 n(\lambda_2)]} \tag{2.1}$$

where λ_1 and λ_2 are the wavelengths corresponding to the two adjacent maxima or minima, and $n(\lambda_1)$ and $n(\lambda_2)$ are the refractive indices at λ_1 and λ_2, respectively. The refractive indices of the titania nanotube film were calculated using the transmittance spectrum in the range 380–1,100 nm by employing Manifacier's envelope method [93]:

$$n(\lambda) = \sqrt{S + \sqrt{S^2 - n_0^2(\lambda) n_S^2(\lambda)}} \tag{2.2}$$

$$S = \frac{1}{2}\left[n_0^2(\lambda) + n_S^2(\lambda)\right] + 2 n_0 n_S \frac{T_{\max}(\lambda) - T_{\min}(\lambda)}{T_{\max}(\lambda) \times T_{\min}(\lambda)} \tag{2.3}$$

where n_0 and n_s are the refractive indices of air and film, respectively, $T_{\max}$ is the maximum envelope, and $T_{\min}$ is the minimum envelope. From the transmittance spectrum, the refractive index of glass is calculated as a function of wavelength using the relation

$$n_s(\lambda) = \frac{1}{T_s(\lambda)} + \sqrt{\frac{1}{T_s^2(\lambda)} - 1} \tag{2.4}$$

where T_s is the transmittance of glass.

Figure 2.23 shows the refractive index of the thin-film titania nanotubes and, for comparison, the glass substrate, calculated using (2.3) and (2.4) [3]. The optical behavior of the TiO_2 nanotube arrays is quite similar to that reported for mesostructured titanium dioxide. The average refractive index of the nanotube array (450°C annealed) was found to be 1.66 in the visible range, 380–800 nm. The thickness, as calculated by inserting the values of refractive indices and the wavelength corresponding to two consecutive maxima or minima (Fig. 2.23) in (2.2), was found to be 340 nm. This agrees with the value of 300 nm for the total thickness of the nanotube array including the barrier layer, determined from FESEM images.

The porosity of the nanotube array architecture was determined from the relation [94]

$$Porosity(\%) = \left[1 - \frac{n^2 - 1}{n_d^2 - 1}\right] \times 100 \tag{2.5}$$

where n (=1.66) and n_d (= 2.5) are the refractive indices of the nanotube structure (annealed at 450°C) and nonporous anatase films, respectively. The porosity of the
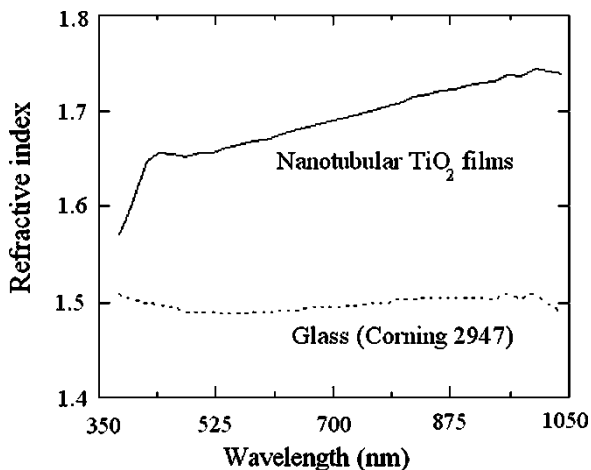
Fig. 2.23 Refractive index variation of 450°C annealed nanotubular titania film and, for comparison, a glass (Corning 2947) substrate, in the range 380–1,050 nm. The TiO$_2$ film has an average refractive index in the visible range of 1.66

nanotube structure was calculated as 66.5%, which is close to the calculated value of 67% for nanotube arrays grown on titanium foil using a 10-V anodization potential [3, 95]. The low refractive index is due to the high porosity of the nanotube architectures, with nanotube diameters much less than the wavelength of light in the visible range, which reduces the light reflection from the surface of the array. The absorption coefficient α and the bandgap E_{g} are related through the equation [96]

$$(\alpha h v)^s = h v - E_{\mathrm{g}} \tag{2.6}$$

where v is the frequency, h is Plank's constant, and $s = 0.5$ for indirect bandgap material. The Tauc plot, $\sqrt{\alpha h v}$ $vs.$ $h v$, obtained after substituting the value of α in this equation is shown in Fig. 2.24 [3]. The optical bandgap, obtained by dropping a line from the maximum slope of the curve to the x-axis, is 3.34 eV. XRD results showed only anatase phase in the transparent titania nanotube array film. The reported bandgap value of anatase phase in bulk is 3.2 eV [97]. A slight blue shift in the value might be due to a quantization effect in the nanotubular film where the wall thickness is about 12 nm. A band tail to 2.4 eV is observed. The degree of lattice distortion is likely to be relatively higher for nanotube array films, thus causing aggregation of vacancies acting as trap states along the seams of nanotube walls leading to a lower band-to-band transition energy.

As seen from the structural studies, nanotube array films that retain an underlying metal layer have anatase-phase nanotube walls and a rutile-phase barrier layer. The absorbance spectra of these opaque films were compared with those of nanotube array films grown on metal foils (both annealed at 480°C) in the wavelength range 320–800 nm, as shown in Fig. 2.25 [3]. Although there is no significant difference between the behavior of thin film and foil samples, the shift in the
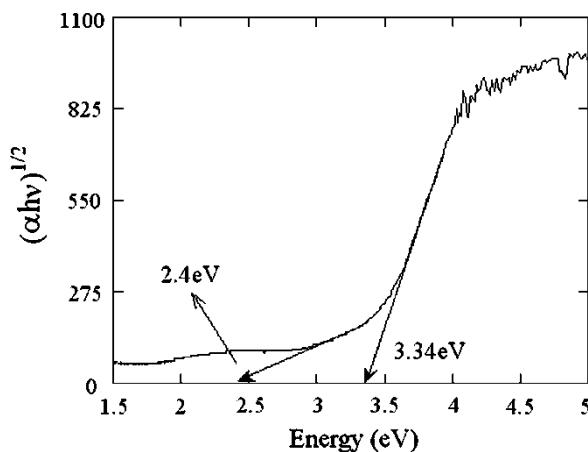
Fig. 2.24 $\sqrt{\alpha\hbar\omega}$ *vs.* $\hbar\omega$ plot of a 450°C annealed nanotube array film. An indirect bandgap of 3.34 eV and band tailing up to 2.4 eV is observed in the film [3]
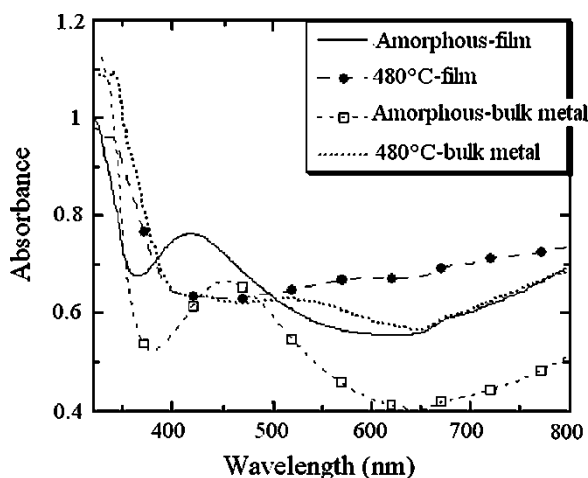
Fig. 2.25 Diffuse reflectance spectra of thin film (with a significant underlying Ti layer) and bulk metal samples, as-anodized (amorphous) and 480°C annealed. Both film and foil samples were prepared in the same electrolyte and annealed under identical conditions [3]

absorption edge towards higher wavelengths on annealing the samples is evident from this figure. The presence of rutile phase, which has a bandgap of ~3.0 eV, makes the absorption edge close to 400 nm [97].

The UV–vis spectra of the electrochemically doped nitrogen and fluorine-doped TiO$_2$ thin films revealed that the presence of fluorine did not result in a discernable change in optical absorption, whereas N-doping exhibited slightly higher optical absorption in the wavelength range from 400 to 510 nm [63]. The optical absorption
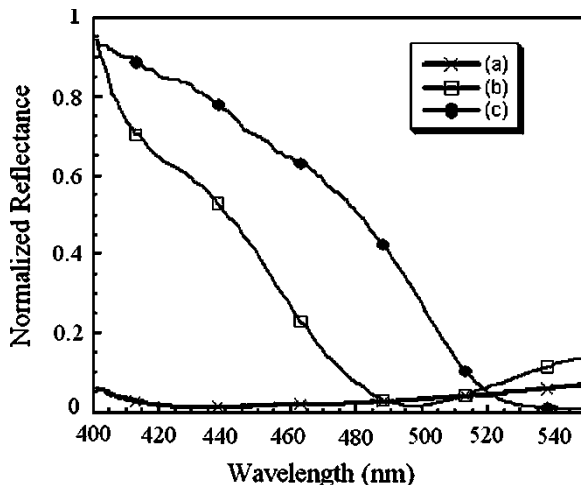
Fig. 2.26 Normalized visible reflectance spectra of CdS–TiO$_2$ nanotube array electrodes. (**a**): TiO$_2$ nanotube array electrode; (**b**) 20 min –0.5 V electrodeposited CdS-modified TiO$_2$ nanotube array electrode, as fabricated; (**c**) electrode of (**b**) after annealing at 350°C for 60 min in N$_2$ [75]

is a function of both film thickness and nitrogen concentration. The film with the highest nitrogen concentration, Sample A with $x=0.23$, is also the thinnest film owing to the fact that it was anodized for only 17 s [63]. The improvement in optical absorption is manifested most clearly for films of similar thickness. All N-doped films exhibited a shift in the primary absorption threshold, with the magnitude of this shift increasing with the concentration of incorporated nitrogen.

Normalized visible reflectance spectra of a plain TiO$_2$ nanotube array electrode as well as CdS-modified TiO$_2$ nanotube array electrodes are shown in Fig. 2.26 [75]. The reflectance onset was determined by linear extrapolation from the inflection point of the curve toward the baseline. The CdS coating on nanotube array has red-shifted the absorption edge into the visible region, with the absorption tail extending to 500 nm; the bandgap calculated from this reflectance edge is about 2.53 eV [75]. After annealing (N$_2$, 350°C, 1 h) its absorption behavior has further red-shifted, with the reflectance tail extending to 515 nm, with a calculated bandgap edge of 2.41 eV; the absorption edge corresponds to a nanoparticle size of approximately 10 to 20 nm [98, 99]. With annealing, the CdS particles aggregate and cause the spectrum to red-shift, a behavior previously attributed to the formation of valence-band tail states [100].

2.4.3 Ellipsometric Measurements

Ellipsometric methods have been used to study the growth process of TiO$_2$ nanotube array films [101]. Changes in ellipsometric parameters (Δ, Ψ) were measured
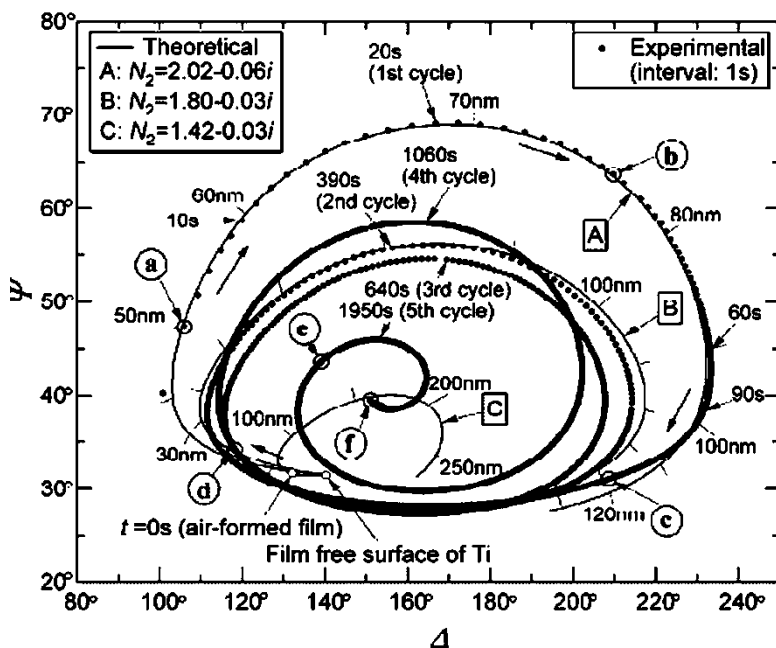
Fig. 2.27 Experimental Δ–Ψ curve for growth of TiO_2 film on Ti at 20 V in 0.5 wt%NH_4F, and theoretical Δ–Ψ curves ([101]; Reprinted by permission of ECS –The Electrochemical Society)

as a function of time during anodization of Ti at 20 V in 0.5 wt%NH_4F. Figure 2.27 shows the experimental Δ,Ψ plot in 0.5 wt%NH_4F and three theoretical Δ–Ψ curves A, B, and C calculated for the growth of single-layer films [101]. The experimental Δ–Ψ plot starts at an initial point determined by the air-formed film and traces out a circular curve that passes repeatedly near the initial point. The experimental Δ–Ψ point for the initial anodization period of 60 s moves at a high speed through the first cycle and fits the theoretical Δ–Ψ curve A calculated for a film with N_2=2.02–0.06i. This indicates that a single-layer film grows rapidly in this period. Beyond 60 s, the experimental Δ–Ψ plot deviates from the theoretical curve A, moving inside theoretical curve A. The experimental Δ–Ψ plot of the next three cycles does not fit a theoretical curve for growth of a single-layer film having a fixed optical constant, but is close to the theoretical curve B calculated for a film with N_2= 1.80–0.03i, which is small compared to the N_2 value used for the calculation of the theoretical curve A (N_2=2.02–0.06i). The experimental Δ–Ψ plot of the fifth cycle deviates from that of the antecedent four cycles, spiraling inward. The experimental plot in this cycle cannot fit a theoretical curve for the growth of a single-layer film but may be simulated by a model in which the refractive index of the film decreases as low as that used for the calculation of the theoretical curve C (N_2=1.42–0.03i).

An optical model was suggested to compare the theoretical Δ–Ψ curves for growth of anodic TiO_2 nanotube layers with the experimental Δ–Ψ curves [101].
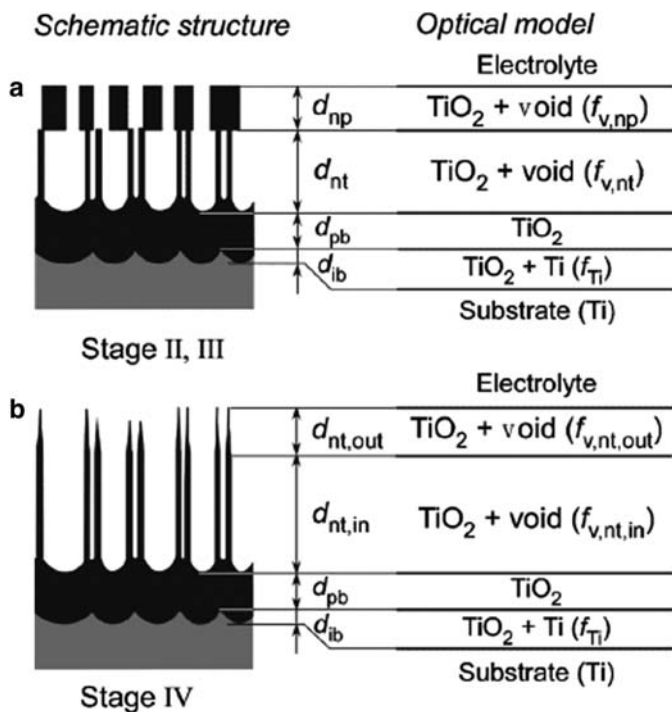
Fig. 2.28 Schematic structure and optical models of TiO$_2$ nanotube layers formed on Ti in NH$_4$F solutions ([101]; Reprinted by permission of ECS –The Electrochemical Society)

Figure 2.28a shows a four-layer optical model employed to calculate the theoretical curves for the films growing in Stage II. Nanoporous and nanotube layers are modeled as a mixture of TiO$_2$ and voids, which are filled with electrolytes. The optical constants of these two layers can be calculated as a function of the void fraction f_v by using the Bruggeman effective medium approximation (EMA) [102]. Because a barrier layer at the bottom of nanotubes is scalloped, this layer can be divided into upper and lower parts, which are called the *pure barrier layer* and *interface barrier layer*, respectively [103]. The pure barrier layer is regarded as pure TiO$_2$ and the interface barrier layer as a mixture of TiO$_2$ and substrate material (Ti). The optical constant of the interface barrier layer can be calculated using the EMA model for a given Ti fraction f_{Ti}. In the Bruggeman EMA, the effective dielectric function ε of a layer consisting of two materials A and B is given by solving the following equations [104]:

$$\left[f_A \frac{(\varepsilon_A - \varepsilon)}{(\varepsilon_A + 2\varepsilon)} \right] + \left[f_B \frac{(\varepsilon_B - \varepsilon)}{(\varepsilon_B + 2\varepsilon)} \right] = 0 \tag{2.7}$$

$$f_A + f_B = 1 \tag{2.8}$$
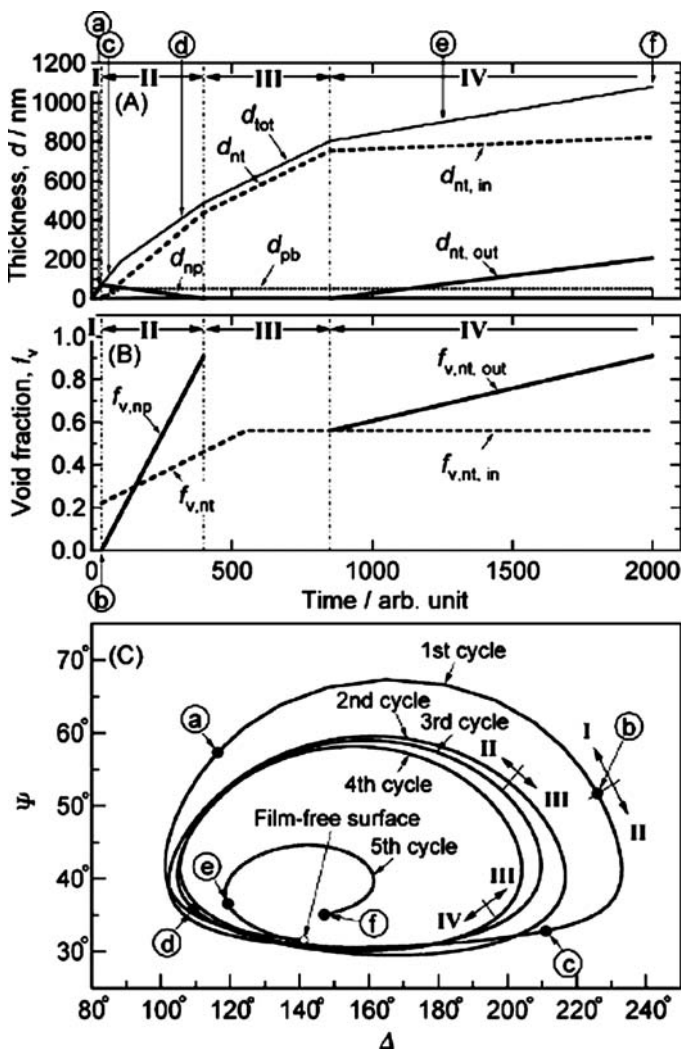
Fig. 2.29 (**a**) Thickness vs. time and (**b**) void fraction vs. time relationships used for model calculation, and (**c**) the resulting calculated Δ–Ψ curve ([101]; Reprinted by permission of ECS – The Electrochemical Society)

where ε_A and ε_B are the dielectric functions of constituents A and B, respectively. f_A and f_B represent the volume fractions of these constituents. The dielectric function can be related to the optical constant N by the following simple equation: $\varepsilon = N^2$. The films in the last growth Stage IV can also be expressed by the four-layer optical model as shown in Fig. 2.28b [101]. In this case, the nanotube layer is separated into two layers with different void fractions $f_{v,nt,out}$ and $f_{v,nt,in}$.

Figure 2.29 exhibits a set of thickness vs. time relations (top), and void fraction vs. time relations (middle) used in a model calculation, and the resulting calculated

Δ–Ψ trajectory (bottom) [101]. The following assumptions were used for the calculation: (i) the initial TiO$_2$ barrier layer grows to 70 nm; (ii) the optical constant of TiO$_2$ material is 2.20–0.00i; (iii) the void fraction of the nanoporous layer $f_{v,np}$ increases linearly from 0 to 0.91 with decreasing thickness of this layer d_{np} from 70 to 0 nm; (iv) the void fraction of the nanotube layer $f_{v,nt}$ increases linearly from 0.22 to 0.56 with increasing thickness of this layer d_{nt} from 0 to 520 nm; (v) the dissolution of the nanotube mouths becomes significant when a certain period of time passes after the surface nanoporous layer disappears and the void fraction of the resulting outer nanotube layer $f_{v,nt,out}$ increases linearly from 0.56 to 0.91 with time; (vi) the thicknesses of the pure and interface barrier layers increase with time in the initial period of oxidation and then remain constant at 50 and 5 nm, respectively; and (vii) the Ti fraction of the interface layer f_{Ti} is kept constant at 0.25. The calculated Δ–Ψ trajectory (Fig. 2.29c) is similar to the experimental Δ–Ψ plot shown in Fig. 2.27 [101].

2.4.4   Raman Spectra Measurements

The different phases of titanium dioxide, i.e., anatase, rutile, and brookite, have characteristic Raman peaks, and hence Raman spectra can be used to demonstrate the effects of calcination temperature on the phase of nanotube array on the Ti substrate. Figure 2.30 shows the Raman spectra of titania nanotube arrays after
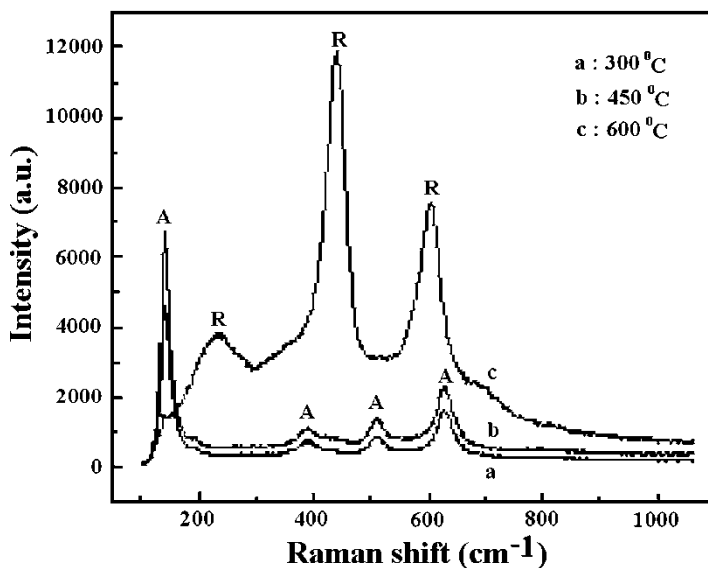
Fig. 2.30 Raman spectra of the TN array calcined at various temperatures, where the peaks representing anatase and rutile are labeled A and R, respectively ([16]; Reprinted by permission of ECS – The Electrochemical Society)

calcination at temperatures ranging from 300 to 600°C [16]. Peaks representing the anatase and the rutile form of TiO_2 are labeled A and R, respectively. Amorphous TiO_2 has no Raman peaks. When the sample was calcined at 300°C, the typical peaks 144, 197, 400, 515, and 640 cm^{-1} corresponding to anatase phase appeared [105]. When the calcination temperature was increased from 300 to 450°C, the peak intensity of anatase increased, which is ascribed to the gradual growth of crystallites and increase in the degree of crystallization. While the temperature was increased to above 450°C, the anatase phase began to transform to the more stable phase of rutile. The Raman spectra showed that rutile (143, 235, 447, and 612 cm^{-1}) became the main phase at 600°C [105]. On observing the Raman spectra of the three samples prepared by different voltages and calcined at 450°C, it was found that the intensity ratio of the anatase peak to the rutile peak increased with the increase in anodization voltage, indicating that the content of anatase phase prepared at 20 V is higher than that of the other two samples [16].

2.5   Electrical Property Measurements

2.5.1   Photocurrent Transient Measurements

The electronic properties of TiO_2 nanotube layers were characterized using photo-current transient measurements [106]. Generated photocurrent transients, the shape of which depends on the crystal state, were recorded when a light pulse at a wavelength of 350 nm was applied for 10 s [106]. For the annealed nanotube layer, an initial rapid increase of the current is recorded, followed by a gradual decrease of the photocurrent with time. The same transient behavior can be observed on compact layers. This behavior was described in terms of a classical onset of recombination. The simplest kinetic approach is based on an exponential law [106]

$$I_{ph}(t) = \left\{ I_{ph}(t = 0) - I_{ph}(t = \infty) \right\} \exp(-kt) + I_{ph}(t = \infty) \qquad (2.9)$$

where k denotes a rate constant. By fitting (2.9) to the experimental data points, the rate constants yield $k = 0.315, 0.393$ and $0.14 \, s^{-1}$ for the as-anodized compact layer, the annealed compact layer, and the annealed nanotube layers, respectively. The rate constant for the annealed compact layer is comparable to that for the as-formed compact layer, contradicting what one might anticipate. For the as-anodized nano-tube layer, the photocurrent continuously increases with time during illumination; it appears trap-filling results in a photocurrent increase. A number of localized states are introduced in the TiO_2 bandgap after anodization, which act as recombination or trap sites. The as-anodized nanotube layer could contain deeper traps due to fluoride-induced etching of the formed oxide. When trap-filling behavior is domi-nant, during illumination over time the traps are filled with photogenerated charge

carriers, which can enhance charge carrier lifetimes. Therefore, the photocurrent gradually increases as the number of filled traps increases. The process may be described by the following kinetic equation [106]:

$$I_{ph}(t) = \{1 - \exp(-kt)\} \cdot \{I_{ph}(t = \infty) - I_{ph}(t = 0)\} + I_{ph}(t = 0) \qquad (2.10)$$

where k denotes a rate constant. Upon fitting (2.10) to the observed data points, the rate constants yield $k = 0.49$ s^{-1} for the as-anodized nanotube layer.

2.5.2   Capacitance Measurements

The semiconducting properties of TiO$_2$ nanotube array/electrolyte interfaces were analyzed by means of impedance spectroscopy near the flat band potential. Three different samples were used; compact layers: 1 M H$_3$PO$_4$ (10 V, 10 min, oxide thickness~25 nm); short e-tubes: 1 M H$_3$PO$_4$+0.3% HF (10 V, 2 h, thickness ~500 nm, pore size 75 nm); and long e-tubes: 1 M NaH$_2$PO$_4$+0.5% HF (20 V, 2 h, thickness ~1 μm, pore size 150 nm) [107, 108]. Thermal annealing of the oxide layers was carried out at 450°C in air during 3 h using a heating and cooling rate of 20°C/s. Acetate and borate buffer solutions of pH 2.73 – 9 were used for the capacitance analysis. Figure 2.31 shows that the cathodic polarization curves performed on compact and porous oxides are characterized by a current plateau followed by an exponential increase at $U < -0.5$ V [107]. This behavior change may be ascribed to the disappearance of the Schottky barrier control with the onset
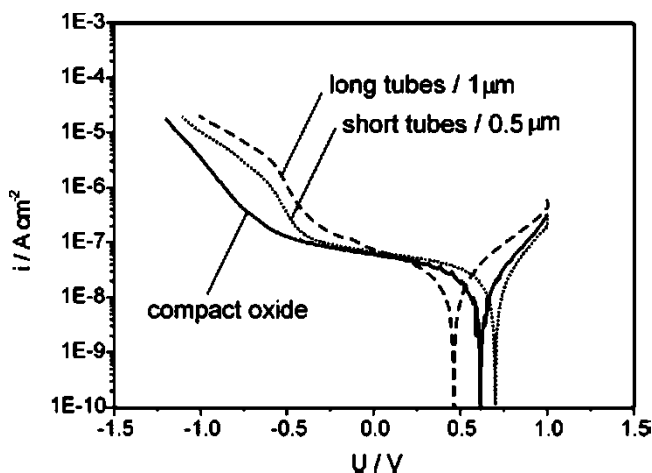
Fig. 2.31 Polarization curves obtained in acetate buffer solution of pH 6 on compact and porous oxides, with a voltage sweep rate of $v = 5$ mVs^{-1}([107]; Copyright 2007. Reprinted with permission from Elsevier)

of a kinetic-controlled electron transfer. However, the presence of an anodic current at potentials between 0.5 and 1 V indicates the start of oxygen evolution promoted by hole injection from the valence band. A marked difference between the current densities of the compact and porous oxides can be observed at a potential $U < -0.5$ V, which is mainly related to the larger active area of the nanotubes. However, practically no differences can be discerned at $U > -0.5$ V, indicating a common controlling step in the charge-transfer mechanism. It is suggested that these features are probably a consequence of a two-film structure, a compact base oxide and a nanotube array overlayer [107].

2.5.2.1   Mott–Schottky Plots: Analysis of Interfacial Properties

The Mott–Schottky equation is a common tool used for characterization of the semiconductor/electrolyte interface [109]. The flat band potential U_{fb} and the donor concentration N_D in a specific electrochemical system can be determined by plotting C_{sc}^{-2} vs. potential U according to

$$C_{sc}^{-2} = \left(\frac{2}{\varepsilon \varepsilon_0 e N_D} \right) \left(U - U_{fb} - \frac{kT}{e} \right) \tag{2.11}$$

where C_{sc} represents the differential capacitance of the space charge layer. The presence of a high concentration of multiple donor levels in the bandgap promotes indirect tunneling of electrons through the semiconductor layer, resulting in a variation of the slope of (2.11) with frequency. This frequency dependence is determined by the distribution of relaxation times for electron emission, which in turn depends on the position of the states relative to the conduction band [110]. At sufficiently low frequencies, the response of a large fraction of the frequency dependent donors is expected, avoiding interferences arising from the double layer response at higher frequencies. Figure 2.32 shows the Mott–Schottky plots obtained at $f = 3$ Hz, where two main features can be seen [107, 108]. First, all curves show a marked change of slope, which is associated with band state ionization. Then, the porous oxides show a marked shift of the linear extrapolation to $C^{-2} = 0$ towards more positive values as compared with the compact oxide. According to (2.11), values of $U_{fb} = -0.725$ V and $U_{fb} = -0.33$ V can be calculated for the compact oxide layer and the 1-μm long nanotube layer, respectively [107]. Donor concentrations $N_D = 4.19 \times 10^{19}$ cm^{-3} and $N_D = 1.63 \times 10^{20}$ cm^{-3} (referenced to the geometrical area) for the compact and the 1-μm long tubes oxide layers, respectively, were estimated from the slope near the flat band potential. Typical values reported for the donor concentration are within 10^{19}–10^{20} cm^{-3} as dependent on sample preparation conditions [111–113]. In spite of very different surface areas, similar slopes are found in both the compact and nanotube array layers, reflecting the concept of a porous oxide layer as two oxide films of different capacitance, the lower of which dominates the total response.
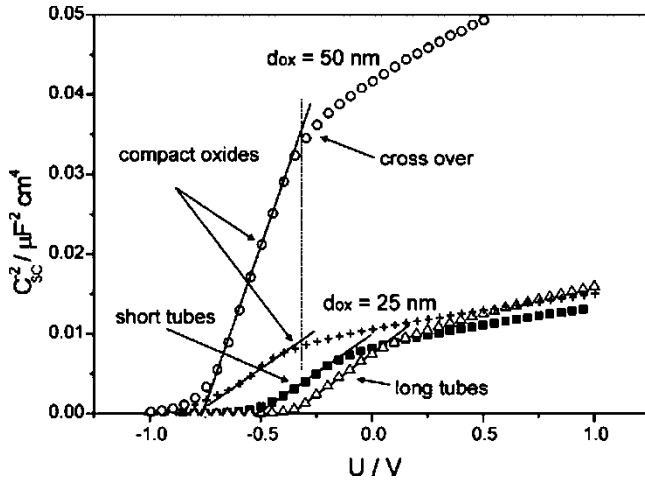
Fig. 2.32 Mott–Schottky plots obtained on compact and porous oxides in acetate buffer solution of pH 6. f=3 Hz; $U_{s,i}$ =1 V ([107]; Copyright 2007. With permission from Elsevier)

The width of a depletion layer in a semiconductor is given by

$$L_D = \left(\frac{2\varepsilon\varepsilon_0}{eN_D}\right)^{1/2} \left(U - U_{fb} - \frac{kT}{e}\right)^{1/2} \tag{2.12}$$

where ε is the dielectric constant of TiO$_2$, taken as 42. This expression predicts a space charge layer thickness of 7 nm at the crossover potential for the 50-nm-thick compact layer formed at 20 V [107]. An alternative interpretation of the impedance responses seen for the anodic semiconductor oxides was introduced by application of amorphous semiconductor theory [114, 115]. According to this model, the capacitance will be given by

$$C_{sc}^{-1} = \frac{1}{\sqrt{\varepsilon\varepsilon_0 eN_D}} \ln \frac{\psi_S}{\psi_C} \tag{2.13}$$

where ψ_S is the band bending and ψ_C corresponds to the maximum polarization for which states still respond. Figure 2.33 shows the inverse of capacitance corresponding to compact and porous oxides [107]; expression (2.13) (solid lines) accurately simulates experimental results after adopting the following values: for compact oxide N_D=3.1 × 10^{20} cm^{-3}eV^{-1}, U_{fb}=−0.85 V and ψ_C=0.15 V; for short tubes N_D=6.5 × 10^{20} cm^{-3}eV^{-1}, U_{fb}=−0.72 V and ψ_C=0.30 V; for long tubes N_D=6.5 × 10^{20} cm^{-3}eV^{-1}, U_{fb}=−0.50 V and ψ_C=0.27 V [107]. It was noted that only the bottom of the porous film responds to the perturbation, and that the pore walls present a highly conducting medium with rather a large contribution due to surface effects (potential drop at the oxide/solution interface). The amorphous-semiconductor theory works well for annealed TiO$_2$ layers which points to a large
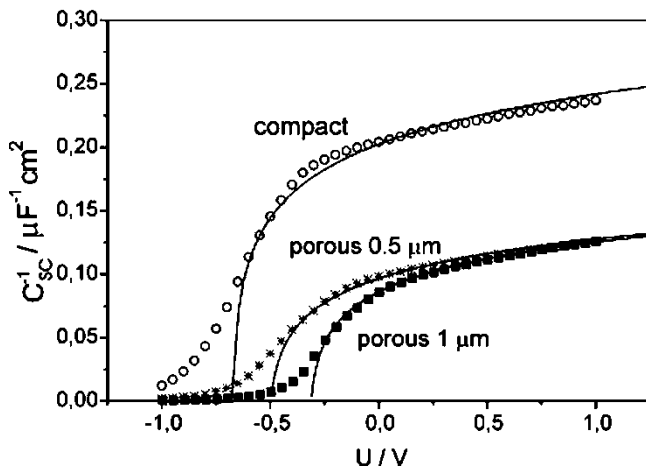
Fig. 2.33 Potential dependence of the inverse of capacitance for annealed compact and porous oxides obtained in acetate buffer solution at $f = 3$ Hz. (—) Fitting curves after (5.5) for the amorphous semiconductor theory ([107]; Copyright 2007. Reprinted with permission from Elsevier)

number of bandgap states, which may be related to mobile defects at $U > U_{\mathrm{fb}}$. Boschloo and coworkers [116, 117] reported the presence of electron traps approximately 0.5 eV below the conduction band as a means to explain the appearance of a photocurrent maximum on zinc-porphyrin-sensitized TiO_2 electrodes. Since the electrode has a large internal area consisting of numerous interconnected nanocrystallites, a high electron trap density is expected at the oxide/electrolyte interface and grain boundaries. Although the chemical origin of these traps is not known, it was suggested that they arise from an incompletely coordinated Ti surface [118].

Interfacial properties of the oxide were further analyzed by the potential dependence of the surface capacitance of compact and porous layers obtained under different solutions and illumination conditions [107]. Without illumination, the Mott–Schottky plots were shifted to more positive potentials with decreasing pH. The pH-dependence of the flat band potential is commonly related to the potential drop at the double layer as a consequence of acid–base reactions

$$TiO_{2\,\mathrm{surface}} + H^+ \leftrightarrow TiO(OH)_{\mathrm{surface}} \tag{2.14}$$

$$TiO(OH)_{\mathrm{surface}} + H^+ \leftrightarrow TiO(OH_2)_{\mathrm{surface}} \tag{2.15}$$
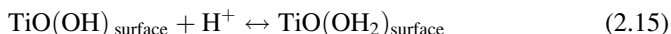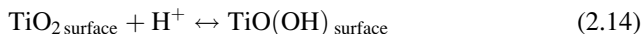
In the absence of surface states and adsorbed ions, the following pH dependence of the flat band potential is expected:

$$U_{\mathrm{fb}} = U_{\mathrm{fb,iep}} - 2.3kT\,(pH - pH_{\mathrm{iep}}) \tag{2.16}$$

where $U_{\mathrm{fb,iep}}$ and pH_{iep} are the flat band potential and the pH at the isoelectric point, respectively, which was found to be 5.8 for anatase [116]. As can be seen in Fig. 2.34,
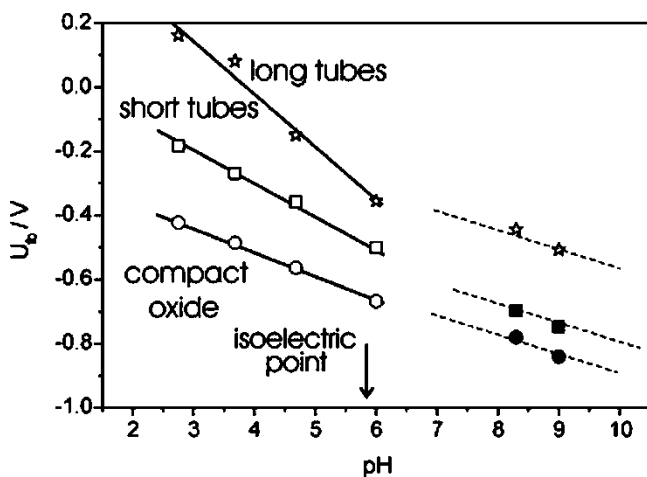
Fig. 2.34 pH dependence of the flat band potential for the different oxides obtained by extrapolation of the low band-bending parts to $C^{-2}=0$ ([107]; Copyright 2007. Reprinted with permission from Elsevier)

this point defines two zones with large deviations of (2.16) at pH < pH$_{iep}$. Slope values of 105 and 166 mV/pH for tube layers 0.5 and 1 μm in length, respectively, are observed, indicating a strong influence of the surface chemistry [107]. Surface charging of TiO$_2$ surfaces in aqueous electrolytes involves not only chemistry of the terminal oxo and hydroxo groups, (2.14) and (2.15), but also the uptake of protons at the band edge trap sites near the flat band potential [119, 120]. Thus, it is feasible that the value of the flat band potential will be mainly determined by equilibration of the conduction band with the trap-based redox couple, which can be written as

$$Ti^{4+}O_2 + H^+ + e^- \rightarrow Ti^{3+}O(OH) \tag{2.17}$$

The displacement towards more positive pH values for the porous layers was interpreted as the natural consequence of a larger density of surface charge and the related Fermi level shift caused on the pore bottoms. It was suggested that the different slopes observed around the isoelectric point were related to pH-dependent surface charging [107], which is related to hydrogen loading in the subsurface region with the formation of incompletely coordinated Ti^{3+} surfaces [121], and interstitial proton and hydroxyl bonds (Ti–O–H) whose formation is favored at pH < pH$_{iep}$.

2.5.2.2   Surface State Model

The pH dependence of the Mott–Schottky plots showed different slopes near the isoelectric point, which may be related to the nature of the surface states, see Fig. 2.34 [107]. It was suggested that surface state formation is related to

incomplete coordination of surface Ti atoms [114], which seems to be favored at $pH < pH_{iep}$. The change of solution pH also affects the donor concentration as can be inferred from the pH dependence of the Mott–Schottky plot slopes. This effect is more pronounced in regions of high band bending, and even more pronounced for oxide layers comprised of short nanotubes [107]. This effect cannot be associated with the reductive effects of hydrogen intercalation, which is observed at a potential more negative than the flat band condition with a consequent marked increase of the donor concentration [116, 117]; hence it appears the effects of pH are largely related to modifications of the surface chemistry [107].

The impedance behavior of the porous structures were interpreted by use of a two-oxide-layer model, with an underlying layer whose behavior can be considered similar to the compact oxide, and where the wall of the oxide tubes presents a higher donor concentration with a consequent higher electronic conductivity than the underlying layer, see Fig. 2.35 [108]. According to this model, with the system under electronic equilibrium, the introduction of the pore walls with a higher donor concentration will shift the energy levels of the compact layer toward higher energies. This, in turn, is reflected by a positive shift of the observed flat band potential [108]. The total capacitance of the oxide will be given by [108]

$$\frac{1}{C_{ox}} = \frac{1}{C_{sc(bottom)}} + \frac{1}{C_{sc(walls)}} \tag{2.18}$$
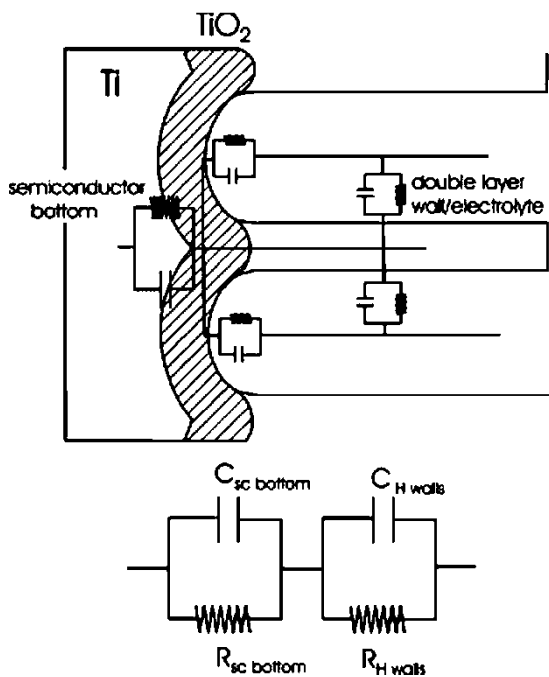
Fig. 2.35 Equivalent circuit representing the impedance response of the porous TiO$_2$ layers ([108]; Copyright Springer-Verlag 2006. With kind permission from Springer Science+Business Media)

Taking into account that C_{sc} is proportional to (N_D) in the depletion region, and that $N_{walls} \gg N_{bottom}$, the observed capacitance response will be dominated by the underlying oxide [108]. Due to the high conductivity of the polycrystalline walls, they can be regarded as an electronic conductor connecting the base semiconductor with the double layer (in solution) [108]. Therefore, the observed response corresponds largely to that of the bottom oxide layer, while the influence of the nanotube arrays is manifest in enhanced surface chemistry effects. The annealing process decreases the defect concentration, and as a consequence the flat band potential shifts toward more positive potentials [108].

The presence of a porous structure on the pH dependence of the flat band potential can also be related to the double-layer semiconductor structure [108]. Here, it is expected that the shift of the Fermi level of the compact oxide will be controlled by the surface chemistry of the pore walls. Thus the noticeable potential shift at pH $<$ 6 in the porous oxide (cf. Fig. 2.34) can be explained in terms of the acid–base reactions of the –OH groups on the surface of the pore walls and the fact that the potential drop seen by the underlying oxide is given by [108]

$$\Delta\phi = \frac{\Delta q A_{pores}}{C A_{bottom}} \qquad (2.19)$$

since part of the surface charge generated in the pore walls must be compensated in the bottom oxide. The presence of these groups would lead to the formation of surface states, the charging of which results in Fermi level pinning.

2.5.2.3 Photoeffects

Surface states lead to trap site formation. Therefore, depending on the relative rates at which the surface states charge and discharge, an additional capacitive element will be built at the interface giving rise to the appearance of a capacitance peak [107]. Electrochemical and spectroscopic experiments have indicated the presence of two intraband surface states in nanotube array films acting as electron traps [116, 118, 121]. These are, respectively, related to adsorbed peroxy or peroxide radicals (located at midgap) and to incomplete coordinated surface Ti atoms in the solid lattice (found to be about 0.8 eV below the conduction band edge). The enhancement of photocurrent after hydrogen loading was observed by Weber et al. [122] on sputtered TiO$_2$ films, which was attributed to the filling of electronic traps by reduction of H$^+$ at the electrode/electrolyte interface. Reductive processes involving hydrogen intercalation were observed at potentials more negative than the flat band condition, with a consequent marked increase of the donor concentration [107, 116, 123, 124].

2.6   Mechanical Properties

The mechanical properties of a material are critical to its successful application [125–127]. This is particularly true in bone-implant materials, where long-term *in vivo* structural stability is crucial. Here, bone resorption occurs due to the mismatch in mechanical properties, such as elastic modulus, between bone and the implant material, causing implant loosening and eventual failure [128]. Considering the drug elution properties of the nanotube array surfaces, discussed in Chap. 6, it is important to characterize the mechanical behavior of these materials for potential use as implants. Furthermore, it is important to establish the relationships between microstructure and mechanical behavior in an effort to elucidate deformation mechanisms.

Mechanical characterization of thin coatings is challenging because of the small length scales involved. In this regard, nanoindentation is an appropriate technique for these materials because of its low load ($1 \mu N$) and small displacement (1 nm) resolution [129]. Nanoindentation is an effective technique for probing mechanical properties of thin ($<10 \mu m$) coated systems including soft coatings on hard substrates [130, 131], hard coatings on soft substrates [132–134], and multilayered systems [132, 135, 136]. This technique has also been used to investigate the mechanical response of TiO_2 with nanophase microstructure [137, 138] and of thin TiO_2 coatings on Ti substrates [133, 134]. Crawford and coworkers carried out a systematic investigation of the microstructure and mechanical behavior of nanotube array films [125], focusing on the relationship between microstructure characterization and deformation behavior by nanoindentation of TiO_2 nanotube array films on Ti substrate. Ti foil was anodized for 2 h in NaF-containing electrolyte (0.1 mol/l F^-), at a pH of 4.5, and constant potential of 20 V. A uniform structure of thin-walled TiO_2 nanotubes was obtained with tube diameters ranging between 35 and 70 nm, tube wall thicknesses between 10 and 18 nm, and tube lengths between 230 and 670 nm [125].

Figure 2.36a shows representative load vs. displacement curves for the samples with varying anodization time [125]. Figure 2.36b shows the extracted apparent Young's modulus and hardness, respectively, obtained from the continuous stiffness measurement (CSM) system [125]. From inspection of Fig. 2.36b, total nanoindentation depth is much larger than the thickness of the coating. In order to gain insight into the underlying deformation mechanisms, SEM of the indentations was conducted. It was noted that coating delamination occurred on unloading only in thin coatings (230–250 nm) and did not occur in thicker coatings (600–650 nm). An additional characteristic of indentations in thicker coatings was wear markings on the indentation surface. These markings suggest some degree of frictional sliding between the indenter and the TiO_2 surface. From FESEM micrographs and the indentation data, two main deformation processes were suggested, densification of the porous nanotube structure and wear of the dense surface.

The deformation mechanisms were correlated to the measured modulus as a function of depth [125], in which three distinct regions were identified [125].
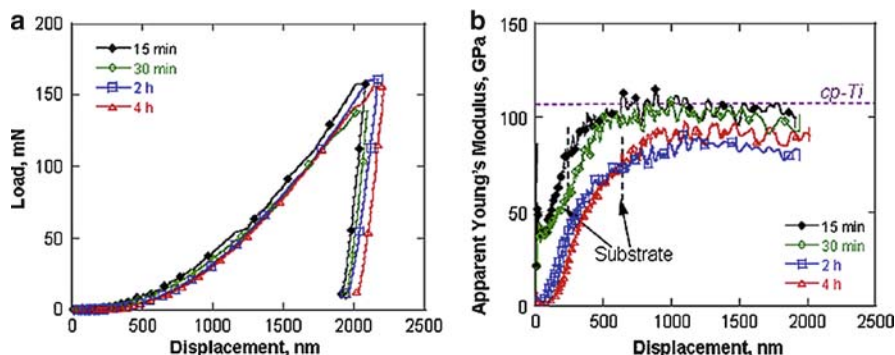
Fig. 2.36 Characteristic (**a**) load and (**b**) apparent Young's modulus vs. nanoindentation displacement (depth) for Ti samples anodized in NaF-containing electrolytes (0.1 mol/l F⁻), at pH 4.5, and constant potential of 20 V for various times ([125]; Copyright 2007. Reprinted with permission from Elsevier)

Region I was characterized by a linear increase in modulus with increasing time. In this region, the increasing modulus is primarily due to increased densification of the TiO₂ nanotubes. A parabolic increase in the indentation modulus was observed in Region II. In this region, the indentation depth is comparable to the thickness of the TiO₂ coating. Thus, increases in modulus were considered as the result of an increasing contribution from the substrate. In addition, there are minor contributions of densification of the outer regions of the indentation and wear between the indenter surface and the dense TiO₂ surface. As the TiO₂ coating under the indenter becomes increasingly dense, the modulus increases. Finally, Region III described the region where the coating has become nearly fully dense. This region was characterized by a plateau in indentation modulus and termed as the composite modulus, as it is a combination of moduli of the dense coating and the Ti substrate. Assuming the volume fraction of pores in the coating of about 72% (estimated from image analyses) and a modulus for dense amorphous TiO₂ of 130–150 GPa (for the tubes themselves) [139], theYoung's modulus for the TiO₂ nanotubes was calculated to be approximately 36–43 GPa [125].

References

1. Varghese OK, Gong D, Paulose M, Ong KG, Grimes CA, Dickey EC (2003) Crystallization and high-temperature structural stability of titanium oxide nanotube arrays. J Mater Res 18:156–165
2. Cai Q, Paulose M, Varghese OK, Grimes CA (2005) The effect of electrolyte composition on the fabrication of self-organized titanium oxide nanotube arrays by anodic oxidation. J Mater Res 20:230–236
3. Mor GK, Varghese OK, Paulose M, Grimes CA (2005) Transparent highly ordered TiO₂ nanotube arrays via anodization of titanium thin films. Adv Funct Mater 15:1291–1296

4. Mor GK, Varghese OK, Paulose M, Shankar K, Grimes CA (2006) A review on highly ordered, vertically oriented TiO₂ nanotube arrays: fabrication, material properties, and solar energy applications. Sol Energy Mater Sol Cells 90:2011–2075

5. Zhao J, Wang X, Sun T, Li L (2005) In situ templated synthesis of anatase single-crystal nanotube arrays. Nanotechnol 16:2450–2454

6. Ghicov A, Tsuchiya H, Macak JM, Schmuki P (2006) Annealing effects on the photoresponse of TiO₂ nanotubes. Phys Stat Sol 203:R28–R30

7. Hahn R, Ghicov A, Salonen J, Lehto VP, Schmuki P (2007) Carbon doping of self-organized TiO₂ nanotube layers by thermal acetylene treatment. Nanotechnol 18:105604 (4pp)

8. Macak JM, Ghicov A, Hahn R, Tsuchiya H, Schmuki P (2006) Photoelectrochemical properties of N-doped self-organized titania nanotube layers with different thicknesses. J Mater Res 21:2824–2828

9. Yang Y, Wang X, Li L (2008) Crystallization and phase transition of titanium oxide nanotube arrays. J Am Ceram Soc 91:632–635

10. Zhao J, Wang X, Sun T, Li L (2007) Crystal phase transition and properties of titanium oxide nanotube arrays prepared by anodization. J Alloys Compd 434–435:792–795

11. Whittemore OJ, Sipe JJ (1974) Pore growth during initial stages of sintering ceramics. Powder Technol 9:159–164

12. Kumar KNP, Keizer K, Burggraaf AJ (1993) Textural evolution and phase-transformation in titania membranes 1. Unsupported membranes. J Mater Chem 3:1141–1149

13. Kumar KNP, Keizer K, Burggraaf AJ, Okubo T, Nagamoto H (1993) Textural evolution and phase-transformation in titania membranes 2. Supported membranes. J Mater Chem 3:1151–1159

14. Macak JM, Tsuchiya H, Schmuki P (2005) High-aspect-ratio TiO₂ nanotubes by anodization of titanium. Angew Chem Int Ed 44:2100–2102

15. Cullity BD, Stock SR (2001) Elements of X-ray diffraction. Prentice-Hall, Englewood Cliffs, NJ

16. Lai Y, Sun L, Chen Y, Zhuang H, Lin C, Chin JW (2006) Effects of the structure of TiO₂ nanotube array on Ti substrate on its photocatalytic activity. J Electrochem Soc 153:D123–D127

17. Chastain J (1992) Handbook of X-ray photoelectron spectroscopy. Perkin-Elmer, Eden Prairie, MN

18. McCafferty E, Wightman JP (1998) Determination of the concentration of surface hydroxyl groups on metal oxide films by a quantitative XPS method. Surf Interface Anal 26:549–564

19. Saha NC, Tomkins HC (1992) Titanium nitride oxidation chemistry – an X-ray photoelectron-spectroscopy study. J Appl Phys 72:3072–3079

20. Marino CEB, Nascente PAP, Biaggio SR, Rocha-Filho RC, Bocchi N (2004) XPS characterization of anodic titanium oxide films grown in phosphate buffer solutions. Thin Solid Films 468:109–112

21. Varghese OK, Paulose M, Shankar K, Mor GK, Grimes CA (2005) Water-photolysis properties of micron-length highly-ordered titania nanotube-arrays. J Nanosci Nanotechnol 5:1158–1165

22. Paulose M, Mor GK, Varghese OK, Shankar K, Grimes CA (2006) Visible light photoelectrochemical and water-photoelectrolysis properties of titania nanotube arrays. J Photochem Photobiol A 178:8–15

23. Ohya Y, Saiki H, Tanaka T, Takahashi Y (1996) Microstructure of TiO₂ and ZnO films fabricated by the sol-gel method. J Am Ceram Soc 79:825–830

24. Shankar K, Mor GK, Prakasam HE, Yoriya S, Paulose M, Varghese OK, Grimes CA (2007) Highly-ordered TiO₂ nanotube-arrays up to 220 μm in length: use in water photoelectrolysis and dye-sensitized solar cells. Nanotechnol 18:065707 (11pp)

25. Yoriya S, Prakasam HE, Varghese OK, Shankar K, Paulose M, Mor GK, Latempa TA, Grimes CA (2006) Initial studies on the hydrogen gas sensing properties of highly-ordered high aspect ratio TiO₂ nanotube-arrays 20 μm to 222 μm in length. Sens Lett 4:334–339

26. Allam NK, Shankar K, Grimes CA (2008) General method for the anodic formation of crystalline metal oxide nanotube arrays without the use of thermal annealing. Adv Mater 20:3942–3946

27. Nishikiori H, Qian W, El-Sayed MA, Tanaka N, Fujii T (2007) Change in titania structure from amorphousness to crystalline increasing photoinduced electron-transfer rate in dye-titania system. J Phys Chem C 111:9008–9011

28. Kondo JN, Domen K (2008) Crystallization of mesoporous metal oxides. Chem Mat 20: 835–847

29. Grimes CA (2007) Synthesis and application of highly ordered arrays of TiO₂ nanotubes. J Mat Chem 17:1451–1457

30. Lee J, Orilall MC, Warren SC, Kamperman M, Disalvo FJ, Wiesner U (2008) Direct access to thermally stable and highly crystalline mesoporous transition-metal oxides with uniform pores. Nature Mater 7:222–228

31. Ohtani B, Ogawa Y, Nishimoto S (1997) Photocatalytic activity of amorphous-anatase mixture of titanium (IV) oxide particles suspended in aqueous solutions. J Phys Chem B 101:3746–3752

32. Demazeau G (2008) Solvothermal reactions: an original route for the synthesis of novel materials. J Mater Sci 43:2104–2114

33. Cushing BL, Kolesnichenko VL, O'Connor CJ (2004) Recent advances in the liquid-phase syntheses of inorganic nanoparticles. Chem Rev 104:3893–3946

34. Roy R (1994) Accelerating the kinetics of low-temperature inorganic syntheses. J Solid State Chem 111:11–17

35. Walton RI (2002) Subcritical solvothermal synthesis of condensed inorganic materials. Chem Soc Rev 31:230–238

36. Mahltig B, Gutmann E, Meyer DC, Reibold M, Dresler B, Günther K, Faßler D, Böttcher H (2007) Solvothermal preparation of metallized titania sols for photocatalytic and antimicrobial coatings. J Mater Chem 17:2367–2374

37. Chen D, Jiao XF, Ritchie RO (2000) Effects of grain-boundary structure on the strength, toughness, and cyclic-fatigue properties of a monolithic silicon carbide. J Am Ceram Soc 83:2079–2081

38. Yoriya S, Mor GK, Sharma S, Grimes CA (2008) Synthesis of ordered arrays of discrete, partially crystalline titania nanotubes by Ti anodization using diethylene glycol electrolytes. J Mater Chem 18:3332–3336

39. Habazaki H, Shimizu K, Nagata S, Skeldon P, Thompson GE, Wood GC (2002) Ionic transport in amorphous anodic titania stabilised by incorporation of silicon species. Corros Sci 44:1047–1055

40. Habazaki H, Shimizu K, Nagata S, Skeldon P, Thompson GE (2007) Fast migration of fluoride ions in growing anodic titanium oxide. Electrochem Commun 9:1222–1227

41. Yu T, Bu H, Chen J (1986) The effect of units derived from diethylene glycol on crystallization kinetics of poly(ethylene terephthalate). Macromol Chem 187:2697–2709

42. Kinart CM, Cwiklinska A, Maj M, Kinart WJ (2007) Thermodynamic and physicochemical properties of binary mixtures of sulfolane with ethylene glycol, diethylene glycol, triethylene glycol, and tetraethylene glycol systems at 303.15 K. Fluid Phase Equilib 262:244–250

43. Cocchi M, Marchetti A, Pigani L, Sanna G, Tassi L, Ulrici A, Vaccari G, Zanardi C (2000) Density and volumetric properties of ethane-1, 2-diol plus di-ethylene glycol mixtures at different temperatures. Fluid Phase Equilib 172:93–104

44. Mor GK, Shankar K, Paulose M, Varghese OK, Grimes CA (2005) Enhanced photocleavage of water using titania nanotube arrays. Nano Lett 5:191–195

45. Park JH, Kim S, Bard AJ (2006) Novel carbon-doped TiO₂ nanotube arrays with high aspect ratios for efficient solar water splitting. Nano Lett 6:24–28

46. Raja KS, Misra M, Mahajan VK, Gandhi T, Pillai P, Mohapatra SK (2006) Photo-electrochemical hydrogen generation using band-gap modified nanotubular titanium oxide in solar light. J Power Sources 161:1450–1457

47. Paulose M, Shankar K, Yoriya S, Prakasam HE, Varghese OK, Mor GK, Latempa TJ, Fitzgerald A, Grimes CA (2006) Anodic growth of highly ordered TiO_2 nanotube arrays to 134 μm in length. J Phys Chem B 110:16179–16184

48. Zhu K, Neale NR, Miedaner A, Frank AJ (2006) Enhanced charge-collection efficiencies and light scattering in dye-sensitized solar cells using oriented TiO_2 nanotubes arrays. Nano Lett 7:69–74

49. Hahn R, Ghicov A, Salonen J, Lehto V, Schmuki P (2007) Carbon doping of self-organized TiO_2 nanotube layers by thermal acetylene treatment. Nanotechnol 18:105604 (4pp)

50. Mohapatra SK, Misra M, Mahajan VK, Raja KS (2007) Design of a highly efficient photoelectrolytic cell for hydrogen generation by water splitting: application of $TiO_{2-x}C_x$ nanotubes as a photoanode and Pt/TiO_2 nanotubes as a cathode. J Phys Chem C 111: 8677–8685

51. Tang XH, Li DY (2008) Sulfur doped highly ordered TiO_2 nanotubular arrays with visible light response. J Phys Chem C 112:5405–5409

52. Vitiello RP, Macak JM, Ghicov A, Tsuchiya H, Dick LFP, Schmuki P (2006) N-Doping of anodic TiO_2 nanotubes using heat treatment in ammonia. Electrochem Commun 8:544–548

53. Lu N, Quan X, Li JY, Chen S, Yu HT, Chen GH (2007) Fabrication of boron-doped TiO_2 nanotube array electrode and investigation of its photoelectrochemical capability. J Phys Chem C 111:11836–11842

54. Mohapatra SK, Misra M, Mahajan VK, Raja KS (2007) A novel method for the synthesis of titania nanotubes using sonoelectrochemical method and its application for photoelectrochemical splitting of water. J Catal 246:362–369

55. Shankar K, Paulose M, Mor GK, Varghese OK, Grimes CA (2005) A study on the spectral photoresponse and photoelectrochemical properties of flame-annealed titania nanotube arrays. J Phys D 38:3543–3549

56. Choi Y, Umebayashi T, Yamamoto S, Tanaka S (2003) Fabrication of TiO_2 photocatalysts by oxidative annealing of TiC. J Mater Sci Lett 22:1209–1211

57. Asahi R, Morikawa T, Ohwaki T, Aoki K, Taga Y (2001) Visible-light photocatalysis in nitrogen-doped titanium oxides. Science 293:269–271

58. Lindgren T, Mwabora JM, Avendano E, Jonsson J, Hoel A, Granvist CG, Lindquist SE (2003) Photoelectrochemical and optical properties of nitrogen doped titanium dioxide films prepared by reactive DC magnetron sputtering. J Phys Chem B 107:5709–5716

59. Kosowska B, Mozia S, Morawski A, Grznil B, Janus M, Kalucki K (2005) The preparation of TiO_2-nitrogen doped by calcination of TiO_2 center dot $xH(2)$ O under ammonia atmosphere for visible light photocatalysis. Sol Energy Mater Sol Cells 88:269–280

60. Wang Y, Feng C, Jin Z, Zhang J, Yang J, Zhang S (2006) A novel N-doped TiO_2 with high visible light photocatalytic activity. J Mol Catal A 260:1–3

61. Ghicov A, Macak JM, Tsuchiya H, Kunze J, Haeublein V, Frey L, Schmuki P (2006) Ion implantation and annealing for an efficient N-doping of TiO_2 nanotubes. Nano Lett 6:1080–1082

62. Ghicov A, Macak JM, Tsuchiya H, Kunze J, Haeublein V, Kleber S, Schmuki P (2006) TiO_2 nanotube layers: dose effects during nitrogen doping by ion implantation. Chem Phys Lett 419:426–429

63. Shankar K, Tep KC, Mor GK, Grimes CA (2006) An electrochemical strategy to incorporate nitrogen in nanostructured TiO_2 thin films: modification of bandgap and photoelectrochemical properties. J Phys D 39:2361–2366

64. Chourasia AR, Chopra DR (1992) X-ray photoelectron spectra of TiN. Surf Sci Spectra 1:233–237

65. Chourasia AR, Chopra DR (1995) X-ray photoelectron study of Tin/SiO_2 and Tin/Si interfaces. Thin Solid Films 266:298–301

66. Yakovleva NM, Anicai L, Yakovlev AN, Dima L, Khanina EY, Buda M, Chupakhina EA (2002) Structural study of anodic films formed on aluminum in nitric acid electrolyte. Thin Solid Films 416:16–23

67. Augustynski J, Berthou H, Painot J (1976) XPS study of interactions between aluminum metal and nitrate ions. Chem Phys Lett 44:221–224

68. Parkhutik VP, Makushok YE, Kudryavtsev VI, Sokol VA, Khodan AN (1987) X-ray photoelectron study of the formation of anodic oxide-films on aluminum in nitric-acid. Sov Electrochem 23:1439–1444

69. Öchsner R, Kluge A, Ryssel H (1989) A versatile ion implanter for material modification. Nucl Instrum Methods B 37–38:504–507

70. Saha NC, Tompkins HG (1992) Titanium nitride oxidation chemistry – an X-ray photoelectron-spectroscopy study. J Appl Phys 72:3072–3079

71. Li J, Lu N, Quan X, Chen S, Zhao H (2008) Facile method for fabricating boron-doped TiO$_2$ nanotube array with enhanced photoelectrocatalytic properties. Ind Eng Chem Res 47:3804–3808

72. Chen D, Yang D, Wang Q, Jiang ZY (2006) Effects of boron doping on photocatalytic activity and microstructure of titanium dioxide nanoparticles. Ind Eng Chem Res 45:4110–4116

73. Zhao W, Ma WH, Chen CC, Zhao JC, Shuai ZG (2004) Efficient degradation of toxic organic pollutants with Ni$_2$O$_3$/TiO$_{2-x}$B$_x$under visible irradiation. J Am Chem Soc 126:4782–4783

74. Ruan C, Paulose M, Varghese OK, Mor GK, Grimes CA (2005) Fabrication of highly ordered TiO$_2$ nanotube arrays using an organic electrolyte. J Phys Chem B 109:15754–15759

75. Chen SG, Paulose M, Ruan C, Mor GK, Varghese OK, Kouzoudis D, Grimes CA (2006) Electrochemically synthesized CdS nanoparticle-modified TiO$_2$ nanotube-array photoelectrodes: preparation, characterization, and application to photoelectrochemical cells. J Photochem Photobiol 177:177–184

76. Kundu M, Khosravi AA, Kulkarni SK (1997) Synthesis and study of organically capped ultra small clusters of cadmium sulphide. J Mater Sci 32:245–258

77. Savelli M, Bougnot J (1979) Topics in applied physics, vol 31. Solar Energy Conversion, Springer, Berlin

78. Mor GK, Varghese OK, Paulose M, Shankar K, Grimes CA (2005) Effect of anodization bath chemistry on photochemical water splitting using titania nanotubes. Mater Res Soc Symp Proc 836:L1.9.1

79. de Taconni NR, Chenthamarakshan CR, Yogeeswaran G, Watcharenwong A, de Zoysa RS, Basit NA, Rajeshwar K (2006) Nanoporous TiO$_2$ and WO$_3$ films by anodization of titanium and tungsten substrates: Influence of process variables on morphology and photoelectrochemical response. J Phys Chem B 110:25347–25355

80. Taflove A (1995) Computational electrodynamics: the finite-difference time-domain method. Artech House Inc, Boston

81. Ong KG, Varghese OK, Mor GK, Grimes CA (2005) Numerical simulation of light propagation through highly-ordered titania nanotube arrays: Dimension optimization for improved photoabsorption. J Nanosci Nanotechnol 5:1–7

82. Roden JA, Gedney SD (1997) Efficient implementation of the uniaxial-based PML media in three-dimensional nonorthogonal coordinates with the use of the FDTD technique. Microwave Opt Technol Lett 14:71–75

83. Wittberg TN, Wolf JD, Keil RG, Wang PS (1983) Low-temperature oxygen diffusion in alpha titanium characterized by auger sputter profiling. J Vac Sci Technol A 1:475–478

84. Negishi N, Takeuchi K, Ibusuki T (1998) Surface structure of the TiO$_2$ thin film photocatalyst. J Mater Sci 33:5789–5794

85. Amanullah FM, Al-Mobarak MS, Al-Dhafiri AM, Al-Shibani KM (1999) Development of spray technique for the preparation of thin films and characterization of tin oxide transparent conductors. Mater Chem Phys 59:247–253

86. Yang P, Liou KN, Mishchenko MI, Gao BC (2000) Efficient finite-difference time-domain scheme for light scattering by dielectric particles: application to aerosols. Appl Opt 39:3727–3737

87. Mor GK, Shankar K, Varghese OK, Grimes CA (2004) Photoelectrochemical properties of titania nanotubes. J Mater Res 19:2989–2996

88. Zheng S, Gao L, Zhang QH, Sun J (2001) Synthesis, characterization, and photoactivity of nanosized palladium clusters deposited on titania-modified mesoporous MCM-41. J Solid State Chem 162:138–141

89. Vogel R, Meredith P, Kartini I, Harvey M, Riches JD, Bishop A, Heckenberg N, Trau M, Rubinsztein-Dunlop H (2003) Mesostructured dye-doped titanium dioxide for micro-optoelectronic applications. Chem Phys Chem 4:595–603

90. Liu FM, Wang TM (2002) Surface and optical properties of films grown by radio frequency nanocrystalline anatase titania reactive magnetron sputtering. Appl Surf Sci 195:284–290

91. Oh SH, Kim DJ, Hahn SH, Kim EJ (2003) Comparison of optical and photocatalytic properties of TiO_2 thin films prepared by electron-beam evaporation and sol-gel dip-coating. Mater Lett 57:4151–4155

92. Asanuma T, Matsutani T, Liu C, Mihara T, Kiuchi M (2004) Structural and optical properties of titanium dioxide films deposited by reactive magnetron sputtering in pure oxygen plasma. J Appl Phys 95:6011–6016

93. Manifacier JC, Gasiot J, Fillard JP (1976) Simple method for determination of optical-constants n, k and thickness of a weakly absorbing thin-film. J Phys E 9:1002–1004

94. Vogel R, Meredith P, Kartini I, Harvey M, Riches JD, Bishop A, Heckenberg N, Trau M, Dunlop HR (2003) Mesostructured dye-doped titanium dioxide for micro-optoelectronic applications. Chem Phys Chem 4:595–603

95. Mor GK, Carvalho MA, Varghese OK, Pishko MV, Grimes CA (2004) A room-temperature TiO_2-nanotube hydrogen sensor able to self-clean photoactively from environmental contamination. J Mater Res 19:628–634

96. Yoldas BE, Partlow DP (1985) Formation of broad-band antireflective coatings on used silica for high-power laser applications. Thin Solid Films 129:1–14

97. Tauc J (1970) Absorption edge and internal electric fields in amorphous semiconductors. Mater Res Bull 5:721–729

98. Sant PA, Kamat PV (2002) Interparticle electron transfer between size-quantized CdS and TiO_2 semiconductor nanoclusters. Phys Chem Chem Phys 4:198–203

99. Henglein A (1989) Small-particle research – physicochemical properties of extremely small colloidal metal and semiconductor particles. Chem Rev 89:1861–1873

100. Kokai J, Rakhshani AE (2004) Photocurrent spectroscopy of solution-grown CdS films annealed in $CdCl_2$ vapour. J Phys D 37:1970–1975

101. Joo S, Muto I, Hara N (2008) In situ ellipsometric analysis of growth processes of anodic TiO_2 nanotube films. J Electrochem Soc 155:C154–C161

102. Bruggeman DAG (1935) Calculation of various physics constants in heterogenous substances. I. Dielectricity constants and conductivity of mixed bodies from isotropic substances. Ann Phys 24:636–664

103. Stein N, Rommelfangen M, Hody V, Johann L, Lecuire JM (2002) In situ spectroscopic ellipsometric study of porous alumina film dissolution. Electrochim Acta 47:1811–1817

104. Wang J, Lin Z (2008) Freestanding TiO_2 nanotube arrays with ultrahigh aspect ratio via electrochemical anodization. Chem Mater 20:1257–1261

105. Bersani D, Antonioli G, Lottici PP, Lopez T (1998) Raman study of nanosized titania prepared by sol-gel route. J Non-Cryst Solids 234:175–181

106. Tsuchiya H, Macak JM, Ghicov A, Räder AS, Taveira L, Schmuki P (2007) Characterization of electronic properties of TiO_2 nanotube films. Corros Sci 49:203–210

107. Muñoz AG (2007) Semiconducting properties of self-organized TiO_2 nanotubes. Electrochim Acta 52:4167–4176

108. Muñoz AG, Chen Q, Schmuki P (2007) Interfacial properties of self-organized TiO_2 nanotubes studied by impedance spectroscopy. J Solid State Electrochem 11:1077–1084

109. Sato N (1998) Electrochemistry at metal and semiconductor electrodes. Elsevier, Amsterdam, The Netherlands

110. Dafonseca C, Ferreira MG, Belo MD (1994) Modeling of the impedance behavior of an amorphous-semiconductor schottky-barrier in high depletion conditions –application to the study of the titanium anodic oxide electrolyte junction. Electrochim Acta 39:2197–2205

111. Oliva FY, Avalle LB, Santos E, Cámara OR (2002) Photoelectrochemical characterization of nanocrystalline TiO$_2$ films on titanium substrates. J Photochem Photobiol A 146:175–188

112. Dolata M, Kedzierzawski P, Augustynski J (1996) Comparative impedance spectroscopy study of rutile and anatase TiO$_2$ film electrodes. Electrochem Acta 41:1287–1293

113. Simons W, Pauwels L, Hubin A (2002) Impedance spectroscopy to characterise an anodised titanium substrate in contact with silver complexing agents: elements for an optimal parameter estimation. Electrochim Acta 47:2169–2175

114. Di Quarto F, La Mantia F, Santamaría M (2005) Physicochemical characterization of passive films on niobium by admittance and electrochemical impedance spectroscopy studies. Electrochim Acta 50:5090–5102

115. Cohen JD, Lang DV (1982) Calculation of the dynamic-response of schottky barriers with a continuous distribution of gap states. Phys Rev B 25:5321–5350

116. Boschloo GK, Goossens A, Schoonman J (1997) Photoelectrochemical study of thin anatase TiO$_2$ films prepared by metallorganic chemical vapor deposition. J Electrochem Soc 144:1311–1317

117. Boschloo GK, Goossens A (1996) Electron trapping in porphyrin-sensitized porous nanocrystalline TiO$_2$ electrodes. J Phys Chem 100:19489–19494

118. Redmond G, Fitzmaurice D, Grätzel M (1993) Effect of surface chelation on the energy of an intraband surface-state of a nanocrystalline TiO$_2$ film. J Phys Chem 97:6951–6954

119. Lyon LA, Hupp JT (1999) Energetics of the nanocrystalline titanium dioxide aqueous solution interface: approximate conduction band edge variations between H–0=−10 and H–=+26. J Phys Chem 103:4623–4628

120. Kavan L, Kratochvilova K, Grätzel M (1995) Study of nanocrystalline TiO$_2$ (anatase) electrode in the accumulation regime. J Electroanal Chem 394:93–102

121. Gutierrez C, Salvador P (1982) Bandgap at the normal-TiO$_2$ electrolyte interface. J Electroanal Chem 138:457–463

122. Weber MF, Schumacher LC, Dignam MJ (1982) Effect of hydrogen on the dielectric and photo-electrochemical properties of sputtered TiO$_2$ films. J Electrochem Soc 129:2022–2028

123. Ghicov A, Tsuchiya H, Hahn R, Macak JM, Muñoz AG, Schmuki P (2006) TiO$_2$ nanotubes: H$^+$ insertion and strong electrochromic effects. Electrochem Commun 8:528–532

124. Fabregat-Santiago F, Barea EM, Bisquert J, Mor GK, Shankar K, Grimes CA (2008) High carrier density and capacitance in TiO$_2$ nanotube arrays induced by electrochemical doping. J Am Chem Soc 130:11312–11316

125. Crawford GA, Chawla N, Das K, Bose S, Bandyopadhyay A (2007) Microstructure and deformation behavior of biocompatible TiO$_2$ nanotubes on titanium substrate. Acta Biomater 3:359–367

126. Katz JL (1996) Application of materials in medicine and dentistry: orthopedic applications. In: Ratner BD, Hoffman AS, Schoen FJ, Lemons JE (eds) Biomaterials Science: An Introduction to Materials in Medicine. San Diego, Academic Press, pp 335–346

127. Park JB, Lakes RS (1992) Biomaterials: an introduction. Plenum Press, New York, pp 79–115

128. Huiskes R, Weinans H, Vanrietbergen B (1992) The relationship between stress shielding and bone-resorption around total hip stems and the effects of flexible materials. Clin Orthop Relat Res 274:124–134

129. Oliver WC, Pharr GM (1992) An improved technique for determining hardness and elastic-modulus using load and displacement sensing indentation experiments. J Mater Res 7:1564–1567

130. Tsui TY, Pharr GM (1999) Substrate effects on nanoindentation mechanical property measurement of soft films on hard substrates. J Mater Res 14:292–2301

131. Tsui TY, Vlassak J, Nix WD (1999) Indentation plastic displacement field: Part I. The case of soft films on hard substrates. J Mater Res 14:2196–2203

132. Tsui TY, Vlassak J, Nix WD (1999) Indentation plastic displacement field: Part II. The case of hard films on soft substrates. J Mater Res 14:2204–2209

133. Bahr DF, Woodcock CL, Pang M, Weaver KD, Moody NR (2003) Indentation induced film fracture in hard film–soft substrate systems. Int J Fract 119:339–349
134. Pang M, Bahr DF (2001) Thin-film fracture during nanoindentation of a titanium oxide film–titanium system. J Mater Res 16:2634–2643
135. Deng X, Cleveland C, Karcher T, Koopman M, Chawla N, Chawla KK (2005) Nanoindentation behavior of nanolayered metal–ceramic composites. J Mater Eng Perform 14:417–423
136. Deng X, Chawla N, Chawla KK, Koopman M, Chu JP (2005) Mechanical behavior of multilayered nanoscale metal–ceramic composites. Adv Eng Mater 7:1099–1108
137. Mayo MJ, Siegel RW, Narayanasamy A, Nix WD (1990) Mechanical properties of nanophase TiO_2 as determined by nanoindentation. J Mater Res 5:1073–1081
138. Han Y, Hong SH, Xu KW (2002) Porous nanocrystalline titania films by plasma electrolytic oxidation. Surf Coat Tech 154:314–318
139. Fischer-Cripps AC (2004) Nanoindentation. Springer, New York